ABSTRACT

Title of Document: POST-SILICON GROUP IV MATERIALS: SELECTED APPLICATIONS OF QUANTUM MECHANICS TO DEVICE SIMULATION

Ittai Baum
Masters of Science, 2019

Directed by: Professor Neil Goldsman
Department of Electrical and Computer Engineering

Quantum mechanics is applied to the study and simulation of two features of group IV semiconductor devices: metal/n-type 4H-SiC interfaces for SiC-based Schottky diodes and GeO_2 gate dielectrics for Ge-based Metal-Oxide-Semiconductor Field-Effect Transistors (MOSFETs).

SiC is well suited for power electronics due to its relatively wide bandgap and high breakdown field. In Schottky power diodes, one consideration in device performance is reverse saturation leakage. For metal/4H-SiC interfaces, reverse saturation leakage current is modeled with quantum transmission calculated by the Symmetrized Transfer Matrix Method (STMM). The classical thermionic emission model and quantum model are compared for multiple donor concentrations. The quantum model is then compared to experimental results for Ti/4H-SiC measurements, and the effect of Fermi pinning is included to account for the correct barrier height. Multiple donor concentrations are again modeled to best fit the bias dependence of the measured curves to find an effective doping level to reflect possible

barrier thinning.

Ge is considered as a possible replacement for Si in MOSFET design as device lengths continue to scale down to match Moore's Law and Si MOSFETs become increasingly difficult to fabricate. Ge is considered due to its relatively high electron and hole mobilities, and its ability to grow a native oxide like Si. However, GeO_2 and the Ge/GeO_2 interface suffer from high defect densities, with one such defect being the oxygen vacancy defect. For GeO_2, the oxygen vacancy defect, and corresponding fluorine passivation, are modeled using Density Functional Theory (DFT) to calculate the atomic configurations and energies. Incorporation of fluorine atoms in the vicinity of the defect is modeled, as well as the incorporation of fluorine atoms within the oxide network. Hydrogen passivation is also modeled and found to not be as energetically favorable. Finally, fluorine diffusion through the oxide network is investigated by calculating the reaction pathway between fluorine incorporation sites in the network.

POST-SILICON GROUP IV MATERIALS: SELECTED APPLICATIONS OF QUANTUM MECHANICS TO DEVICE SIMULATION

By

Ittai Baum

Thesis submitted to the Faculty of the Graduate School of the
University of Maryland, College Park, in partial fulfillment
of the requirements for the degree of
Masters of Science
2019

Examining Committee:
Professor Neil Goldsman, Chair
Professor Kevin Daniels
Professor Alireza Khaligh

© Copyright by
Ittai Baum
2019

Dedication

To my Aba and Ima

Acknowledgments

I would like to thank everyone who supported me during this time and who provided me with energy and motivation.

First I would like to thank Prof. Goldsman for his support and guidance during my experience at the University of Maryland. He continually pushed me to expand my horizons and engage in new ways of thinking. I believe I have learned a lot these past few years because of him and I am very grateful to have had him as my advisor. Without him, none of this would have been possible.

I would like to express my appreciation and gratitude towards Prof. Kevin Daniels and Prof. Alireza Khaligh for taking the time out of their busy schedules to serve on my examining committee.

I would like to thank George Metze from the Laboratory for Physical Sciences, College Park, MD and Aivars Lelis from the Army Research Laboratory, Adelphi, MD for their support.

I would like to thank Mitchell Gross, Aysanew Abate, Dr. Akin Akturk and Dr. Zeynep Dilli for their experimental work and the measurements they took that supplemented my research.

I would like to thank my friends and colleagues from the lab- Chris Darmody, Yumeng Cui, Christian Xiao, Alex Mazzoni and Franklin Nouketcha - for their interesting discussions and comradery during my time at the University of Maryland. They made me feel welcome when I arrived, and provided me with essential guidance that allowed me to complete this work.

I would like to my friends from home, Sebi Medina-Tayac, David Rico, Ami Smerling, Julian Lofton, Sid Nanda, Maureen Lei, and Gabe Koempel. They helped make my days enjoyable and provided me with plenty of happiness and encouragement.

I would like to thank my girlfriend Neil Marino for their continual love and support during this time. They were always supportive of whatever path I chose, and was there for me when I needed them most. Without them, this final leg of the journey would have been much more difficult.

And finally I would like to thank my family. My sister, Maya, for our discussions that helped me understand this time in my life. My parents, Noa and Stuart, for always being there for me and providing me with so much it is impossible to list here. Their love and support were critical for me to start and finish this entire journey, and I will never be able to fully express how grateful I am towards them.

Table of Contents

Table of Contents v

List of Tables vii

List of Figures viii

1 Introduction 1
- 1.1 The Search for Alternatives to Silicon 1
  - 1.1.1 Power Diodes: Silicon-Carbide (SiC) 1
  - 1.1.2 High Mobility MOSFETs: Germanium (Ge) 3

2 Power Diodes: Silicon Carbide 5
- 2.1 Basic Properties of Silicon Carbide 5
  - 2.1.1 Crystal Structure 5
  - 2.1.2 Electrical Properties 10
- 2.2 4H-SiC Schottky Power Diode 11
  - 2.2.1 Modeling Reverse Current Leakage 12
    - 2.2.1.1 The Potential Energy Barrier 12
    - 2.2.1.2 Derivation of Leakage Current Formula 16
    - 2.2.1.3 Transmission Coefficient Calculation 21
  - 2.2.2 Fermi Level Pinning 31
  - 2.2.3 Theory vs. Experiment 34
    - 2.2.3.1 Effective Doping Level 37
- 2.3 Future Research 41

3 High Mobility MOSFETs: Germanium 42
- 3.1 Background Overview 42
  - 3.1.1 Basic Properties of Germanium 42
    - 3.1.1.1 Crystal Structure 42
    - 3.1.1.2 Electrical Properties 42
  - 3.1.2 Oxide/Semiconductor Interfaces 43
    - 3.1.2.1 Si/SiO_2 Interface Structure 44
    - 3.1.2.2 Ge/GeO_2 Interface Structure 45
    - 3.1.2.3 Volatility of Ge/GeO_2 interface 46
    - 3.1.2.4 Interface Defects 48
  - 3.1.3 Density Functional Theory 48

3.1.3.1 Motivation . . . 48
3.1.3.2 Kohn-Sham Equations . . . 50
3.1.3.3 Application of DFT . . . 51
3.2 Current Research . . . 52
3.2.1 DFT Simulations of Bulk Supercells: Ge, GeO_2, and Ge/GeO_2 interface . . . 54
3.2.1.1 Bulk Ge . . . 55
3.2.1.2 Bulk GeO_2 . . . 58
3.2.2 DFT Simulations of Defects and Passivation . . . 62
3.2.2.1 Oxygen Vacancy . . . 62
3.2.2.2 Fluorine Passivation of Oxygen Vacancy . . . 65
3.2.2.3 Diffusion of Fluorine in GeO_2 . . . 71
3.3 Future Research . . . 75

A Density Functional Theory 76
A.1 Born-Oppenheimer Approximation . . . 76
A.2 Hohenberg-Kohn Theorems . . . 77

Bibliography 79

List of Tables

2.1 Effective masses in 4H-SiC, in units of m_0 the free electron mass [36] 8

3.1 Comparison of calculated values to experimental values for GeO_2 α-quartz 60

List of Figures

2.1 Stacking sites for SiC polytypes indicated with A,B and C, as viewed from the (0001) plane. The first stacking plane is indicated by A, with sites arranged hexagonally. The B and C sites then refer to two distinct stacking arrangements relative to the A sites. [34] 6
2.2 Hexagonal Bravais lattice with the four lattice vectors and (0001) and $(000\bar{1})$ faces depicted. For SiC, the (0001) face is denoted the Si-face and the $(000\bar{1})$ is denoted the C-face. [39] 7
2.3 Stacking arrangement of 4H-SiC. The grouping of the bilayer is depicted such that each bilayer has an atomic Si layer and C layer. [35] 7
2.4 The hexagonal unit cell of 4H-SiC. C atoms are depicted in red and Si atoms are depicted in blue. [41] 8
2.5 Brillouin zone of 4H-SiC. The high symmetry points and and irreducible wedge are depicted. [38] 9
2.6 Brillouin zone of 4H-SiC viewed from the (0001) direction. The three equivalent valleys are depicted with ovals, each valley is centered on the M high symmetry point. [40] 10
2.7 Potential energy qϕ(x) of a Schottky contact under reverse bias V_R with IFBL (blue) and without (black dashed). On the right is the semiconductor and on the left is the metal. E_F denotes the Fermi level of the metal, and E_{Fn} denotes the electron quasi-Fermi level in the semiconductor. ϕ_{B0} indicates the barrier height without IFBL and ϕ_B indicates the barrier height with IFBL, which is a function of the applied bias. x_n indicates the depletion width and is also a function of the applied bias. qϕ_n is the potential difference between the conduction band and the quasi-Fermi level in the semiconductor. V_{bi} is the built-in potential. 14
2.8 Incident wave A with wavenumber k_I scattering of a barrier, with reflected component B and transmitted component C 21
2.9 Cartoon depiction of the discretized potential (in red) to the true potential (in blue). Mesh points and half-mesh points are indicated. 24

2.10 Transmission coefficient through 0.62 eV Schottky barrier with different donor doping levels for an applied reverse bias of (top) 0.6 V and (bottom) 10 V. The classical step function is also graphed in dashed line alongside to indicate barrier value 28
2.11 Differential current density through a 0.62 eV barrier for a doping concentration of 10^{16} cm^{-3} at an applied reverse bias of 0.6 V is calculated using the classical and quantum models. The reduction in current in the quantum model is due to quantum reflection. 29
2.12 Differential current density through a 0.62 eV barrier calculated for different doping concentrations at an applied reverse bias of 10 V. . . 30
2.13 Current density through a 0.62 eV Barrier for different doping concentrations, with the quantum models (solid) plotted against the classical models (dashed) for comparison. The variation in the classical models is due to IFBL 32
2.14 Measured leakage current through Ti on n-type 4H-SiC Schottky barrier is graphed for different diodes in the unbolded curves. Bolded curves are from theoretical calculations using a doping concentration of 10^{16} cm^{-3}, using Fermi pinned barriers equal to the respective defect energy and for two ideal metal barriers, Ti and Ni. 35
2.15 Average error between theoretical currents for different doping levels and measured current in the (top) higher current group and (bottom) lower current group 38
2.16 Best fit theoretical current curves graphed alongside a measured curve from the (top) higher and (bottom) lower current groups. For each comparison, the three best fit doping levels were used. 39

3.1 Section of 73 atom supercell of amorphous GeO_2 with a peroxyl defect. Peroxyl O atoms are highlighted in green, Ge atoms in purple, regular O atoms labeled in red. 47
3.2 Flowchart depicting the three main steps in the DFT calculation: The atomic coordinates are used to generate the electron density via a nested self-consistent loop that utilizes the Kohn-Sham equations and effective Kohn-Sham potential v_{KS}. The density is used to calculate the atomic forces via the Hellman-Feynman theorem [57]. The atomic forces are then applied to each atom to find the change in the coordinates. The algorithm loop follows the logic of the Born-Oppenheimer approximation, where the change in the electron density and change in atomic coordinates can happen separately, as the electrons respond to changes in the atomic coordinates over a much smaller time scale. 53
3.3 8 atom FCC unit cell of bulk Ge. 55
3.4 Density of States (DOS) plot of Ge using a hybrid functional to reproduce the correct band gap. 56

3.5 Calculated band gap of Ge with increasing Brillouin zone sampling size. Sampling size was increased by incrementally increasing the dimensions of the mesh grid. 56
3.6 18 atom unit cell used to simulate Ge substrate surface. Hydrogen atoms are included to satisfy the dangling bonds on the final layer. Positions of H atoms are held fixed during relaxation to simulate bulk. 57
3.7 Supercell of multiple copies of surface unit cell. The dimer structures are clearly visible, forming rows with channels in between. The buckling of the dimers is seen to alternate parity progressing down the row. 58
3.8 Isosurface Electron Localization Function (ELF) plotted on supercell of surface dimers. Isosurface is of an ELF of 0.8. The ELF indicates the localization of charge. Ge atoms are labeled with purple. Isosurface is labeled with yellow. The isosurface between atoms represents localization due to bonds. The large protrusion at the surface represents the completed sp^3 orbitals. 59
3.9 9 atom unit cell of GeO_2 in the α-quartz polytype. Ge atoms are labeled with purple and O atoms are labeled with red. 59
3.10 72 atom supercell of amorphous GeO_2 formed by applying SBB method with 3 passes to a 72 atom supercell of α-quartz GeO_2. Ge atoms are labeled with purple and O atoms are labeled with red. 61
3.11 71 atom supercell of amorphous GeO_2 with an oxygen vacancy (indicated with black arrow). Ge atoms are labeled with purple and O atoms are labeled with red. 63
3.12 Reaction pathway of oxygen vacancy migration. Steps in the reaction pathway are plotted according to energy difference relative to the final configuration. Energy barrier is given at maximum. Ge atoms are labeled with purple and O atoms are labeled with red. 65
3.13 Sample of initial configurations of F_2 by an oxygen vacancy in a 71 atom amorphous GeO_2 supercell with varying distance to the defect. Ge atoms are labeled in purple, O atoms in red, F atoms in silver. Analogous initial configurations were used in the H_2 case. 67
3.14 Close up of target region of final relaxed structures of 2 H (top) or F (bottom) atoms incorporated into a defected 71 atom amorphous GeO_2 supercell. Ge atoms are labeled in purple, O atoms in red, F atoms in silver, H atoms in blue. On the left are the improper passivations, where one of the H (or F) atoms are bonded to an O atom, leaving a doubly-coordinated Ge atom. On the right are the proper passivations, with the Ge-Ge bond eliminated and replaced with Ge-H (or F) bonds. 68
3.15 Final relaxed structure of 72 (73) atom amorphous GeO_2 supercell with a half (fully) passivated oxygen vacancy by 1 (2) F atom(s). Ge atoms are labeled in purple, O atoms in red, F atoms in silver. On the left is the half passivated vacancy, on the right is the fully passivated vacancy. 70

3.16 Final relaxed structure of an F atom placed into a 72 atom amorphous GeO_2 supercell. Ge atoms are labeled in purple, O atoms in red, F atoms in silver. The F atom has incorporated into the oxide network via bonding with Ge atoms. The Ge atoms are 5-coordinated. 72
3.17 Close up of final relaxed structure of 2 F atoms placed into a 72 atom amorphous GeO_2 supercell. Ge atoms are labeled in purple, O atoms in red, F atoms in silver. On the left image the F atoms are relaxed in interstitial configurations, which were found to be unstable for the 1 F atom case. On the right, the F atoms have incorporated into the oxide network via bonding with Ge atoms. The Ge atoms are 5-coordinated. 74

Chapter 1: Introduction

1.1 The Search for Alternatives to Silicon

For over half a century, the semiconductor industry has been dominated by silicon. Silicon's ability to grow a native stable, insulating oxide was a key component towards developing modern integrated circuit technology, as it allows for multiple devices to be fabricated in close proximity on chip, as well as allow for self-aligned fabrication, and perhaps most importantly, it is a crucial ingredient in metal-oxide-semiconductor field-effect transistors (MOSFETS). While silicon has been the industry standard in almost all domains, from CMOS technology, to power electronics, as device sizes continue to shrink, it is becoming more difficult for new silicon technologies to keep up with the pace set by Moore's Law. One possible solution to this difficulty is to replace silicon with alternative semiconductors that each perform better in different regimes where silicon has reached its limit.

1.1.1 Power Diodes: Silicon-Carbide (SiC)

In the realm of power electronics, SiC is one of the preferred replacements for Si. SiC has excellent material properties that make it well-suited for applications in

power electronics, such as a wide bandgap and high breakdown field. One application in particular that this work focuses on is the use of SiC for power schottky diodes. Schottky diodes are of interest in power electronics because of their relatively higher switching speed than p-n junction diodes, a critical parameter in power conversion technology.

In power applications, the electric fields generated across devices can become quite large, especially in regions such as the metal/semiconductor interface found in Schottky diodes when they are under reverse bias. Since SiC has a breakdown field many times greater than Si, SiC Schottky diodes can hold off much larger voltages under reverse bias. Another important feature in power diodes is the barrier height, which determines how much current can flow through the device. Proper barrier heights can then be engineered by selecting the appropriate metal. However, the presence of defects have been found to lower the barrier height [48] [45], resulting in larger than expected leakage currents. The concentration of defects is irregular and results in barrier height inhomogeneities, with the most severe barrier lowering occurring when high density defect clusters are present. As the area of the diodes increases, so does the probability of a defect cluster appearing. This is especially problematic for power applications, since large area devices are needed to handle the high current output.

When modeling the leakage current, due to the shape of the barrier, the inclusion of quantum mechanical effects will have a non-negligible correction to the current. During high reverse biases, or under high doping concentrations, the large electric field at the interface results in a thin barrier that leads to quantum tunneling.

At low doping concentrations, while tunneling can be negligible, another quantum effect, quantum reflection, will actually reduce the current that would be expected from classical models, an effect that cannot be captured with semi-classical techniques such as the Wentzel-Kramers-Brillouin (WKB) approximation [43]. While some models have used drift-diffusion based models [20] [21], such expensive models were deemed unnecessary for this work as only diodes under reverse bias were considered. In this case, the total current is low enough that the potential barrier will not be significantly altered from the depletion approximation.

1.1.2 High Mobility MOSFETs: Germanium (Ge)

Ge-based transistors are a viable candidate to replace current transistors for a number of reasons: Ge has a higher carrier mobility than Si, so equivalently sized Ge transistors will be able to operate at faster switching speeds than their Si counterparts [1]. The ratio between electron and hole mobility is smaller in Ge than it is in Si, which makes it very attractive for CMOS technology, where a smaller ratio translates to a more efficient use of chip space.

While other materials also boast higher bulk mobilities than Si, Ge also has the advantage of having a native oxide, which allows for an oxide interface to be grown rather than deposited during fabrication. Deposited oxide interfaces have a higher surface roughness than grown oxide interfaces, which degrades mobility. Therefore grown oxide interfaces are more desirable for achieving high surface mobility.

However, the full potential of Ge-based transistors has yet to be realized, as

the oxide/semiconductor interfaces still suffer from high defect densities, trapped charge and high surface roughness, among of other issues, all of which degrade the channel surface mobility [1] [2] [3] [4]. Many of the challenges facing realizing high quality oxide/semiconductor interfaces in Ge stems from having a more reactive interface than in Si [5] [6]. More defects are produced at the interface, and due to Ge in general forming weaker bonds than Si, the defects are able to migrate at quicker rates, yielding unstable oxides and poorly defined interfaces [2] [4] [5] [6] [7]. Various fabrication techniques have been applied to lower the interface defect density in Ge/GeO_2 and $Ge/high-\kappa$ dielectric interfaces, using techniques ranging from high pressure oxidation [3] [9] to fluorine passivation [8] [10].

To understand these challenges, and to find possible solutions to them, I have utilized Density Functional Theory (DFT) to model atomic configurations present in the oxide.

Chapter 2: Power Diodes: Silicon Carbide

2.1 Basic Properties of Silicon Carbide

Silicon carbide is a wide bandgap group IV semiconductor that shares a number of properties with silicon. Having a wider bandgap makes SiC better suited for applications in power electronics. Since SiC is a compound semiconductor, describing its crystal structure is more complicated than it is for Si.

2.1.1 Crystal Structure

SiC is composed of Si and C atoms in a 1:1 stoichiometric ratio, with each Si atom bonded to four C atoms and vice versa. The four bonds from each atom form a regular tetrahedron, just like in Si and carbon diamond lattices. The bonds occupy hybridized sp^3 orbitals and have a bond length of 1.89 Å, with the overall density of SiC being 3.2 g/cm^{-3}.

Various polytypes exist for SiC, distinguished by the specific stacking configurations. The atomic layers of SiC can be grouped into bilayers composed of an atomic Si layer and C layer. The stacking configurations then refer to how the bilayers are stacked relative to each other. There are three distinct stacking sites,

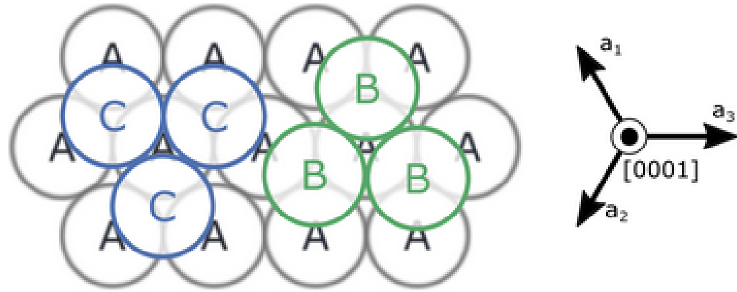

Figure 2.1: Stacking sites for SiC polytypes indicated with A,B and C, as viewed from the (0001) plane. The first stacking plane is indicated by A, with sites arranged hexagonally. The B and C sites then refer to two distinct stacking arrangements relative to the A sites. [34]

denoted A,B and C, depicted in figure 2.1 [34]. The A layer is always the first layer, with lattice sites arranged hexagonally. The individual stacking configurations are then denoted as AB,ABC,ABAC, etc., where the pattern is assumed to repeat (So AB refers to ABABABAB... and so on)

The polytype of interest in this work is 4H-SiC, due to its exceptional electrical properties that will be described in the next section. The H refers to the hexagonal unit cell of the crystal, depicted in figure 2.2 [39]. The (0001) face is referred to as the Si-face (as it composed of Si atoms) and likewise the $(000\bar{1})$ face is referred to as the C face. The 4 refers to the specific stacking configuration, in that the stacking sequence has a length of 4, denoted as ABAC. A side view of the stacking configuration is depicted in figure 2.3 [35] where the bilayers have been sectioned off. Note that simply removing an atomic Si layer from the Si-face, while revealing an atomic C layer, does not produce a C-face, as the newly revealed C atoms are directly above the next layer of Si atoms, whereas on a C-face, the C atoms are

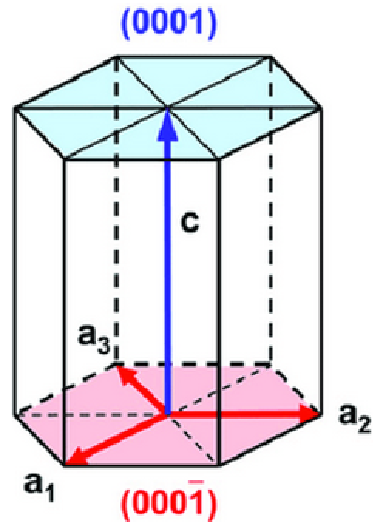

Figure 2.2: Hexagonal Bravais lattice with the four lattice vectors and (0001) and $(000\bar{1})$ faces depicted. For SiC, the (0001) face is denoted the Si-face and the $(000\bar{1})$ is denoted the C-face. [39]

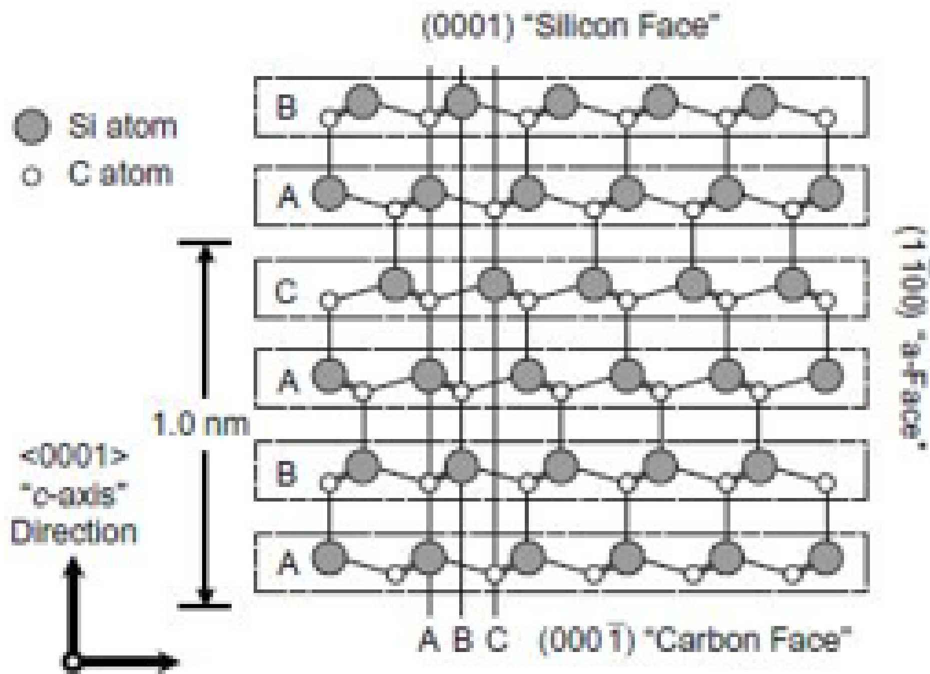

Figure 2.3: Stacking arrangement of 4H-SiC. The grouping of the bilayer is depicted such that each bilayer has an atomic Si layer and C layer. [35]

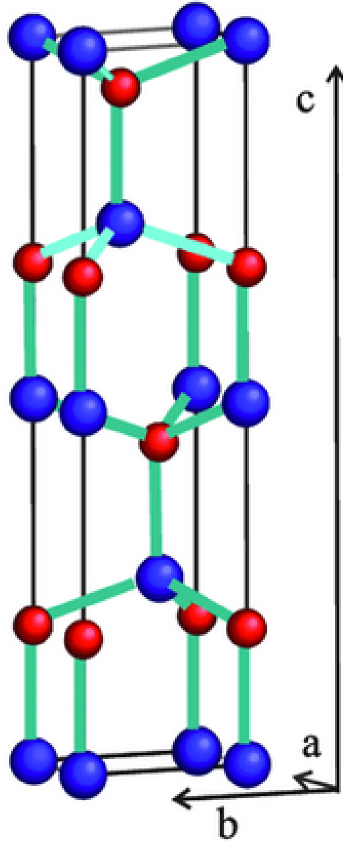

Figure 2.4: The hexagonal unit cell of 4H-SiC. C atoms are depicted in red and Si atoms are depicted in blue. [41]

askew relative to the next layer of Si atoms. The full hexagonal unit cell is depicted in figure 2.4 [41]. Si-face wafers are the most commercially available wafers [37], and so this orientation will be assumed throughout.

$m_{M\Gamma}$	m_{MK}	m_{ML}
0.58	0.31	0.33

Table 2.1: Effective masses in 4H-SiC, in units of m_0 the free electron mass [36]

The Brillouin zone of 4H-Si also has a hexagonal unit cell, depicted in figure

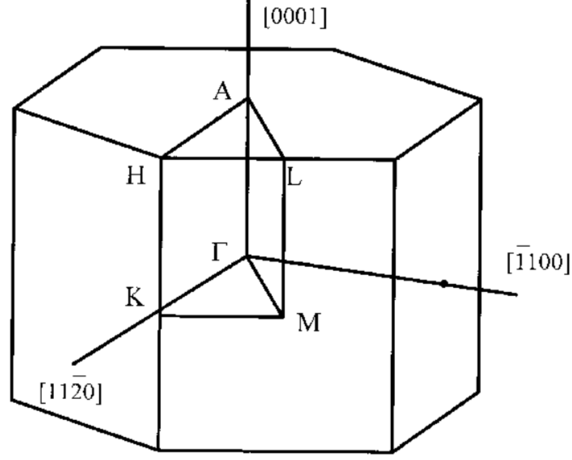

Figure 2.5: Brillouin zone of 4H-SiC. The high symmetry points and and irreducible wedge are depicted. [38]

2.5 [38], where the high symmetry points and irreducible wedge have been indicated. A view from the (0001) direction of the cell is depicted in figure 2.6 [40], where the three equivalent valleys are indicated, with each valley centered on the M high symmetry point. The corresponding effective masses for each direction is given in table 2.1 [36]. For the remainder of this paper, the direction into the Si-face will be the x-direction and the orthogonal plane will be the y-z plane. The effective masses that will be used in the derivations in the section are m_x, m_y and m_z, which are given by:

$$m_x = m_{ML} \tag{2.1}$$

$$m_y = m_z = \frac{2}{\frac{1}{m_{M\Gamma}} + \frac{1}{m_{MK}}} \tag{2.2}$$

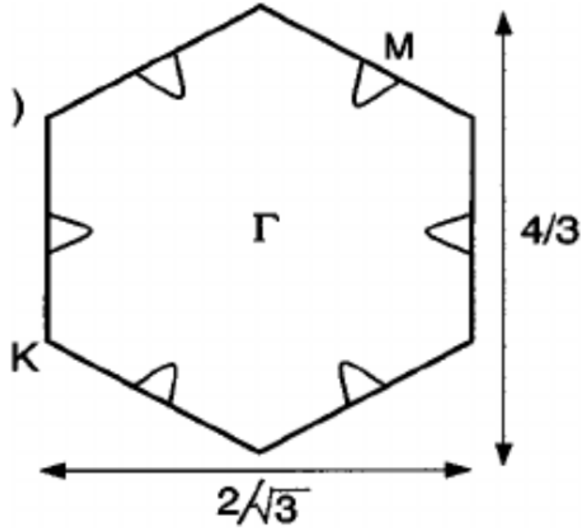

Figure 2.6: Brillouin zone of 4H-SiC viewed from the (0001) direction. The three equivalent valleys are depicted with ovals, each valley is centered on the M high symmetry point. [40]

2.1.2 Electrical Properties

4H-SiC is a wide bandgap semiconductor with a bandgap of 3.2 eV, which make it very attractive for high power electronics. With a wide bandgap, 4H-SiC sports a higher critical field over Si, with a value of about $E_c = 3$ MV/cm, over an order of magnitude higher than the value for Si (about 300 kV/cm) [49] [50]. This allows for device lengths to be scaled down significantly, as high voltages can be dropped across shorter distances without causing excessive impact ionization. 4H-SiC is also preferred over the other polytypes because of its higher electron mobility, with a value as high as 900 cm^2/Vs [50].

The electrical application of 4H-SiC that this work focuses on is towards power diodes. Power diodes are typically Schottky diodes due to Schottky diodes higher

switching speed than p-n junction diodes. High switching speeds are very important in power electronics, such as in power conversion applications. For example, in a boost converter, a Schottky diode will be placed in parallel with a MOSFET that has a high frequency AC signal coming into the gate, rapidly switching the MOSFET on and off. As the MOSFET switches between states, the charge in the channel and drift region must be charged and discharged within the duty cycle of the gate signal. Without the diode present, the MOSFET would charge and discharge via diffusion into the substrate body, which is typically quite slow. The presence of the diode offers another avenue for current to flow, and allows for rapid charging and discharging. In the off state, the drain voltage will be quite high and the diode will be heavily reverse biased. Here the diode must be able to sustain the large electrical field that is formed at the metal/semiconductor interface without breaking down, which is one of the reasons SiC is an attractive choice. Also during the off state, the amount of current leaking through the diode must be kept at a minimum. Since the voltage is so high, any current that leaks through will result in a significant power loss.

2.2 4H-SiC Schottky Power Diode

4H-SiC has promising applications for Schottky power diodes due to its ability to hold off large voltages over short device lengths. However, there are numerous considerations that still need to be addressed, such as high reverse current leakage caused by Fermi pinning due to surface defects.

2.2.1 Modeling Reverse Current Leakage

The dominant component in SiC schottky diode reverse current leakage is due to quantum tunneling when the doping is high enough, as even though the barrier height is large enough to hold off thermionic emission, at large reverse bias voltages the barrier becomes thin enough that tunneling becomes substantial. When the doping is low enough, tunneling will not be too large, and in fact other quantum effects, notably quantum reflection, will reduce the leakage current that would be expected under classical models. Therefore, to accurately calculate leakage current, a quantum model is considered.

2.2.1.1 The Potential Energy Barrier

To model the tunneling current in n-type 4H-SiC Schottky diode, a number of assumptions were taken:

First the potential energy of the barrier was modeled using the depletion approximation, with the inclusion of a term to account for image force barrier lowering (IFBL). The total potential takes the following form at a given reverse bias of V_R, in terms of 'x', the distance from the metal/SiC interface :

$$q\phi(x) = \begin{cases} \frac{qV_{bi} + qV_R}{x_n^2}(x - x_n)^2 + q\phi_n - qV_R + E_F - \frac{q^2}{16\pi\epsilon_{SiC}x}, & 0 < x \leq x_n \\ q\phi_n - qV_R + E_F, & x_n \leq x \end{cases} \tag{2.3}$$

where the first term is the depletion approximation term and the last term is the IFBL term [22], with x_n equal to the depletion width given by:

$$x_n = \sqrt{\frac{2\epsilon_{SiC}(V_{bi} + V_R)}{qN_d}} \tag{2.4}$$

where q is the charge of the electron, ϵ_{SiC} is the dielectric constant of 4H-SiC, N_d is the donor doping concentration and V_{bi} is the built-in potential equal to

$$V_{bi} = \phi_{B0} - \phi_n \tag{2.5}$$

where ϕ_{B0} is the potential barrier height without IFBL, equal to the difference between the conduction band at the interface without IFBL and the Fermi level of the metal, denoted as E_F, and whose value is calculated in a manner described in a later section. ϕ_n is the potential difference between the conduction band in the substrate and the Fermi level of the semiconductor, such that the following equation is satisfied [51]:

$$N_d = \int_0^{+\infty} \frac{4\pi(2m^*)^{3/2}}{h^3} \frac{u^{1/2}}{1 + e^{u + \phi_n / k_B T}} du \tag{2.6}$$

with k_B being the Boltzmann constant, T the temperature, h is Planck's constant and m^* is the effective density of states mass for 4H-SiC. The integration variable, u, represents the difference in energy from the conduction band. This equation applies to degenerate and non-degenerate doping cases.

All variables described here are indicated in figure 2.7, which depicts an ex-

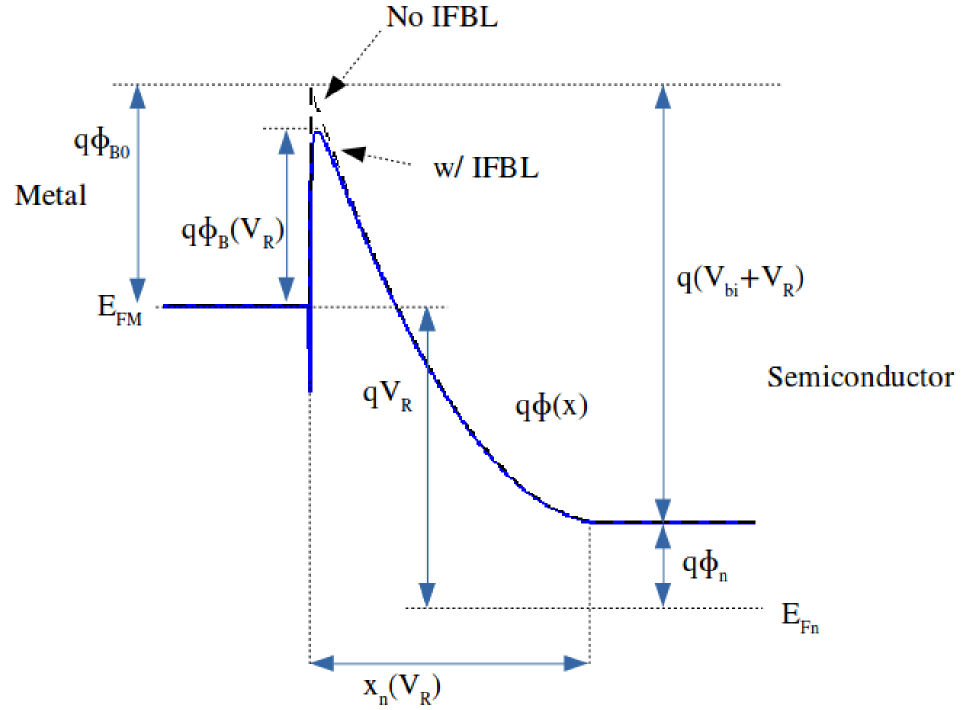

Figure 2.7: Potential energy qϕ(x) of a Schottky contact under reverse bias V_R with IFBL (blue) and without (black dashed). On the right is the semiconductor and on the left is the metal. E_F denotes the Fermi level of the metal, and E_{Fn} denotes the electron quasi-Fermi level in the semiconductor. ϕ_{B0} indicates the barrier height without IFBL and ϕ_B indicates the barrier height with IFBL, which is a function of the applied bias. x_n indicates the depletion width and is also a function of the applied bias. $q\phi_n$ is the potential difference between the conduction band and the quasi-Fermi level in the semiconductor. V_{bi} is the built-in potential.

ample of a Schottky contact barrier under an applied bias, which is what will be considered in this section. The potential energy with and without the inclusion of the IFBL term are depicted, as well as the resulting lowered barrier, equal to [52]:

$$\phi_B(V_R) = \phi_{B0} - \Delta\phi(V_R) \tag{2.7}$$

where

$$\Delta\phi(V_R) = \frac{q}{\epsilon_{SiC}}\sqrt{\frac{x_n N_d}{4\pi}} \tag{2.8}$$

The dependence of the change in the barrier height on bias comes from the depletion width dependence, and will increase with increasing applied reverse bias. In some calculations, the effect of IFBL is entirely included by explicitly using this effective barrier height. However, since some of the calculations described in this chapter will involve the actual shape of the potential and not just the barrier height, the full Coulombic IFBL term is included in the calculations, and the effective barrier height ϕ_B will be considered implicitly.

Another assumption was that, since reverse bias leakage is being modeled, the current flowing through the barrier would be relatively low and the deviation from the depletion approximation would be minimal. Thus a full drift-diffusion solver was not necessary to calculate the potential energy barrier and accurately model the leakage current.

2.2.1.2 Derivation of Leakage Current Formula

Classically, the current flowing through the Schottky barrier is modeled using thermionic emission i.e. thermalized majority carriers from the metal or semiconductor substrate with sufficient energy will flow across the barrier. To calculate the total current density due to thermionic emission, first the following integral is computed for the current due to electrons (since n-type semiconductors are assumed) flowing from the metal to the semiconductor (where the x-coordinate direction is assumed to be parallel with the current flow):

$$J_{MS} = -q \int \int \int_{-\infty}^{+\infty} \frac{2}{(2\pi)^3} \frac{\hbar k_x}{m_x} \frac{1}{1 + e^{(E - E_F)/k_B T}} \Theta(E_x - (q\phi_B + E_F)) dk_x dk_y dk_z \quad (2.9)$$

Where the first term is simply the density of states in k-space (with the factor of 2 included for spin), the second term being the velocity into the barrier, the third term is the Fermi-Dirac statistic, where E is the energy equal to:

$$E = \frac{\hbar^2}{2} (\frac{k_x^2}{m_x} + \frac{k_y^2}{m_y} + \frac{k_z^2}{m_z}) \quad (2.10)$$

and the final term is the Heaviside step function, meant to indicate the classical transmission function, where only electrons with energies higher than the barrier will contribute to the current, with E_x meaning:

$$E_x = \frac{\hbar^2 k_x^2}{2m_x} \quad (2.11)$$

To evaluate the integral, the orthogonal coordinates (the y-z coordinates) to the current are integrated out first. A simple rescaling is implemented at the beginning of the integration to simplify the problem:

$$k'_y = \frac{m_{yz}^{1/2}}{m_y^{1/2}} k_y \tag{2.12}$$

$$k'_z = \frac{m_{yz}^{1/2}}{m_z^{1/2}} k_z \tag{2.13}$$

where

$$m_{yz} = (m_y m_z)^{1/2} \tag{2.14}$$

The corresponding Jacobian is then unity:

$$dk_y dk_z = dk'_y dk'_z \tag{2.15}$$

With the new rescaled variables, the y-z integral is recast into polar coordinates with

$$k_r^2 = k_y'^2 + k_z'^2 \tag{2.16}$$

so that E is now

$$E = \frac{\hbar^2}{2}\left(\frac{k_x^2}{m_x} + \frac{k_r^2}{m_{yz}}\right) \tag{2.17}$$

The integral is now equal to:

$$J_{MS} = q \int_{-\infty}^{+\infty} \int_{0}^{+\infty} \int_{0}^{2\pi} \frac{2}{(2\pi)^3} \frac{\hbar k_x}{m_x} \frac{k_r}{1 + e^{E\,-\,E_F/k_B T}} \Theta(E_x - (q\phi_B + E_F)) dk_\theta dk_r dk_x \tag{2.18}$$

Since there is no angular dependence, the θ-integral evaluates to 2π. After rearranging terms, the integral becomes:

$$J_{MS} = 2\pi q \int_{-\infty}^{+\infty} \frac{2}{(2\pi)^3} \frac{\hbar k_x}{m_x} [\int_{0}^{+\infty} \frac{k_r}{1 + e^{\frac{\hbar^2 k_r^2}{2 m_{yz} k_B T}} e^{E_x\,-\,E_F/k_B T}} dk_r] \Theta(E_x - (q\phi_B + E_F)) dk_x \tag{2.19}$$

The integral inside the bracket can be evaluated exactly as follows (variable substitutions are used for compactness):

$$[\text{integral}] = \int_{0}^{+\infty} \frac{t}{1 + A e^{at^2}} dt = \int_{0}^{+\infty} \frac{t e^{-at^2}}{e^{-at^2} + A} dt \tag{2.20}$$

where

$$t = k_r \tag{2.21}$$

$$a = \frac{\hbar^2}{2 m_{yz} k_B T} \tag{2.22}$$

$$A = e^{E_x\,-\,E_F/k_B T} \tag{2.23}$$

A change of variables then leads to the evaluation:

$$\int_0^{+\infty} \frac{te^{-at^2}}{e^{-at^2}+A}dt = \int_A^{1+A} \frac{1}{2au}du = \frac{1}{2a}ln(1+A^{-1}) \tag{2.24}$$

$$u = e^{-at^2} + A \tag{2.25}$$

$$-\frac{1}{2a}du = te^{-at^2}dt \tag{2.26}$$

The final integral is now (with E_x replacing k_x):

$$J_{MS} = \frac{4\pi q m_{yz} k_B T}{h^3} \int_0^{+\infty} ln(1 + e^{E_F\ -\ E_x/k_BT})\Theta(E_x - (q\phi_B + E_F))dE_x \tag{2.27}$$

Often the barrier height ϕ_B exceeds k_BT/q, and the logarithm in the integral can be Taylor expanded to first order, reducing the integral to [53]:

$$J_{MS} = \frac{4\pi q m_{yz} k_B T}{h^3} \int_{E_F+q\phi_B}^{+\infty} e^{E_F\ -\ E_x/k_BT}dE_x = A^*T^2e^{-q\phi_B/k_BT} \tag{2.28}$$

where

$$A^* = \frac{4\pi q m_{yz} k_B^2}{h^3} = 145.6 A/cm^2K^2 \tag{2.29}$$

is the Richardson's constant. To get the current flowing from the semiconductor to the metal, J_{SM}, the above process is repeated, only the Fermi level in the Fermi-Dirac statistic is replaced with $E_F + qV_a$, where qV_a is the applied bias

(positive for forward, negative for reverse). The semiconductor to metal current is then:

$$J_{SM} = \frac{4\pi q m_{yz} k_B T}{h^3} \int_{E_F+q\phi_B}^{+\infty} e^{E_F - qV_R - E_x/k_B T} dE_x = A^* T^2 e^{-q(\phi_B + V_R)/k_B T} \tag{2.30}$$

The total current is then:

$$J_{TOT(Classical)} = J_{SM} - J_{MS} = A^* T^2 e^{-q\phi_B/k_B T}(e^{-qV_R/k_B T} - 1) \tag{2.31}$$

To upgrade this expression from a classical one to a quantum mechanical one, all that needs to be done is the classical transmission function $\Theta(E)$ is replaced with a quantum mechanical transmission function $\mathbf{T}(E)$ (boldfaced to distinguish it from temperature T). Quantum mechanics predicts that there is a non-zero probability of finding particles in regions of potential energy greater than the particle energy, which is classically forbidden. If a potential energy barrier is thin enough, there is a relatively significant probability of finding the particle on the other side of the barrier, and the particle is said to have tunneled through the barrier. Thus even if $\phi_B >> k_B T$ there could be a significant number of particles contributing to the current near the Fermi level, and so the above Taylor expansion of the logarithm is no longer valid. The full expression for the current now reads:

$$J_{QM} = \frac{4\pi q m_{yz} k_B T}{h^3} \int_0^{+\infty} ln(\frac{1 + e^{E_F - qV_R - E_x/k_B T}}{1 + e^{E_F - E_x/k_B T}})\mathbf{T}(E_x) dE_x \tag{2.32}$$

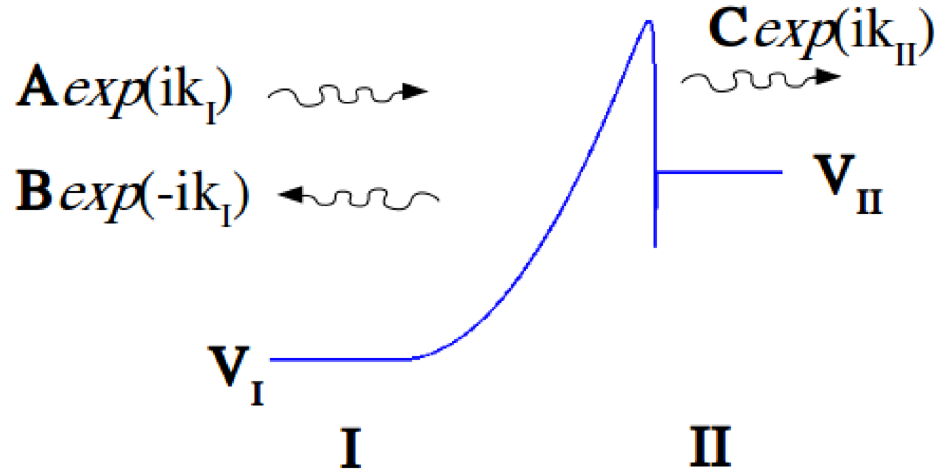

Figure 2.8: Incident wave A with wavenumber k_I scattering of a barrier, with reflected component B and transmitted component C

2.2.1.3 Transmission Coefficient Calculation

To calculate the transmission coefficient $\mathbf{T}(E)$, first the wavefunction for the particle at a given energy must be calculated using the Schrodinger equation. For a given energy E, the Schrodinger equation in 1-D reads:

$$E\Psi = H\Psi = -\frac{\hbar^2}{2m^*}\frac{\partial^2}{\partial x^2}\Psi - q\phi\Psi \tag{2.33}$$

where Ψ is the wavefunction of the particle, and H is the Hamiltonian operator, equal to the sum of the kinetic energy and potential energy operators, $\hbar$ is the reduced planck's constant, and m^* is the effective mass of the particle.

When the potential is at a constant value V, if the energy E is greater than V, the solution to eq. (3.6) reveals the state of the particle is that of a free traveling

wave and Ψ takes the form:

$$\Psi(x) = \mathbf{A}e^{ikx} + \mathbf{B}e^{-ikx} \tag{2.34}$$

where the wavenumber k is equal to

$$k = \frac{\sqrt{2m^*(E-V)}}{\hbar} \tag{2.35}$$

and $\mathbf{A}$ and $\mathbf{B}$ are the amplitudes of the right- and left-traveling waves, respectively.

When calculating tunneling probabilities across a potential barrier, the potential on either side of the barrier is assumed constant, as depicted in figure 2.8, and $V_I - V_{II}$ is equal to the bias applied across the barrier. In region **I**, Ψ is equal to:

$$\Psi(x) = \mathbf{A}e^{ik_Ix} + \mathbf{B}e^{-ik_Ix} \tag{2.36}$$

and in region **II** Ψ is equal to:

$$\Psi(x) = \mathbf{C}e^{ik_{II}x} + \mathbf{D}e^{-ik_{II}x} \tag{2.37}$$

In the case of a wave incident on the barrier coming from the left, **A** represents the amplitude of the incident wave, **B** the amplitude of the reflected wave, and **C** the amplitude of the transmitted wave. Since no wave is assumed to be traveling from the right, **D** is set equal to 0.

The transmission coefficient **T** i.e. the tunneling probability, is defined as the

relative flux between the transmitted wave and the incident wave, where the flux J of a traveling wave Ψ with wavenumber k is given by:

$$J = \frac{\hbar k}{m^*}|\Psi|^2 \tag{2.38}$$

so that $\mathbf{T}$ is equal to:

$$\mathbf{T} = \frac{k_{II}}{k_I}\frac{|\mathbf{C}|^2}{|\mathbf{A}|^2} = \frac{k_{II}}{k_I}|\mathbf{C}|^2 \tag{2.39}$$

where $\mathbf{A}$ has been set equal to 1 since only the relative values of the amplitudes are physically meaningful.

In order to calculate $\mathbf{C}$, the wavefunction inside the barrier must be computed, which involves solving eq. (3.6). One such method that is both computationally efficient and accurate is the Symmetrized Transfer Matrix Method (STMM) [44].

STMM is implemented as follows:

A mesh grid is placed over the barrier region with N mesh points x_j where $j = 1, ..., N$, and $N-1$ mesh spacings Δ_j, with

$$\Delta_j = x_{j+1} - x_j \tag{2.40}$$

An approximate discretely-valued barrier potential Φ is utilized in eq. (3.6) instead of ϕ, depicted in figure 2.9, defined as

$$\Phi(x) = \phi(x_j), \text{when } x_j - \frac{\Delta_{j-1}}{2} < x \leq x_j + \frac{\Delta_j}{2} \tag{2.41}$$

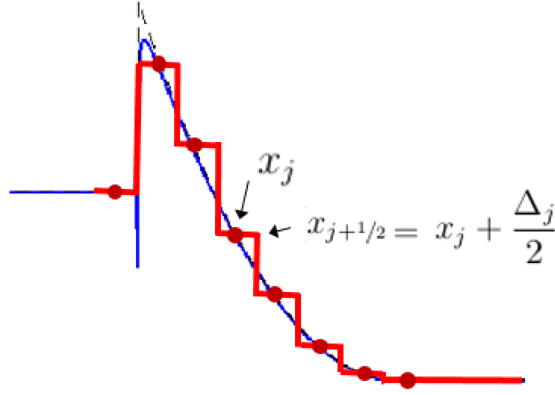

Figure 2.9: Cartoon depiction of the discretized potential (in red) to the true potential (in blue). Mesh points and half-mesh points are indicated.

so that the discontinuities in Φ occur at the half meshpoints.

Since at almost every position Φ is constant, the solution, Ψ, to eq.(3.6) for a given energy E is

$$\Psi(x) = A_j e^{ik_j(x-x_j)} + B_j e^{-ik_j(x-x_j)}, \text{when } x_j - \frac{\Delta_{j-1}}{2} < x \leq x_j + \frac{\Delta_j}{2} \tag{2.42}$$

where

$$k_j = \frac{\sqrt{2m^*(E - \phi(x_j))}}{\hbar} \tag{2.43}$$

In order to compute complex coefficients A_j and B_j, an observation of eq.(3.6) should be made: Since the laplacian of Ψ is defined wherever the potential is defined, Ψ must be differentiable, and therefore also continuous, at every position. This leads

to a system of equations that must be solved at every half meshpoint $x_{j+1/2}$:

$$\Psi_j(x_{j+1/2}) = \Psi_{j+1}(x_{j+1/2}) \tag{2.44}$$

$$\left.\frac{d\Psi_j}{dx}\right|_{x_{j+1/2}} = \left.\frac{d\Psi_{j+1}}{dx}\right|_{x_{j+1/2}} \tag{2.45}$$

$$\begin{aligned} A_j e^{ik_j(x_{j+1/2}-x_j)} + B_j e^{-ik_j(x_{j+1/2}-x_j)} &= A_{j+1} e^{ik_{j+1}(x_{j+1/2}-x_{j+1})} \\ &\quad + B_{j+1} e^{-ik_{j_1}(x_{j+1/2}-x_{j+1})} \qquad (2.46) \\ k_j A_j e^{ik_j(x_{j+1/2}-x_j)} - k_j B_j e^{-ik_j(x_{j+1/2}-x_j)} &= k_{j+1} A_{j+1} e^{ik_{j+1}(x_{j+1/2}-x_{j+1})} \\ &\quad - k_{j+1} B_{j+1} e^{-ik_{j_1}(x_{j+1/2}-x_{j+1})} \end{aligned} \tag{2.47}$$

where the former equation is due to continuity of Ψ and the latter is due to differentiability of Ψ. Rewritten as a matrix equation, the equations take the form:

$$\begin{pmatrix} e^{ik_j\Delta_j/2} & e^{-ik_j\Delta_j/2} \\ k_j e^{ik_j\Delta_j/2} & -k_j e^{-ik_j\Delta_j/2} \end{pmatrix} \begin{pmatrix} A_j \\ B_j \end{pmatrix} = \begin{pmatrix} e^{-ik_{j+1}\Delta_j/2} & e^{ik_{j+1}\Delta_j/2} \\ k_{j+1} e^{-ik_{j+1}\Delta_j/2} & -k_{j+1} e^{ik_{j+1}\Delta_j/2} \end{pmatrix} \begin{pmatrix} A_{j+1} \\ B_{j+1} \end{pmatrix} \tag{2.48}$$

Inverting the matrix on the l.h.s., eq. (3.19) can be expressed compactly as:

$$\begin{pmatrix} A_j \\ B_j \end{pmatrix} = S_j \begin{pmatrix} A_{j+1} \\ B_{j+1} \end{pmatrix} \tag{2.49}$$

where the transfer matrix S_j is

$$S_j = \frac{1}{2} \begin{pmatrix} \frac{k_j^+}{k_j} e^{-ik_j^+ \Delta_j/2} & \frac{k_j^-}{k_j} e^{-ik_j^- \Delta_j/2} \\ \frac{k_j^-}{k_j} e^{ik_j^- \Delta_j/2} & \frac{k_j^+}{k_j} e^{ik_j^+ \Delta_j/2} \end{pmatrix} \tag{2.50}$$

with

$$k_j^+ = k_j + k_{j+1} \tag{2.51}$$

$$k_j^- = k_j - k_{j+1} \tag{2.52}$$

The first and last set of coefficients can then be related via a total transfer matrix S_{TOT}:

$$\begin{pmatrix} A_1 \\ B_1 \end{pmatrix} = S_{TOT} \begin{pmatrix} A_N \\ B_N \end{pmatrix} \tag{2.53}$$

where

$$S_{TOT} = S_1 S_2 ... S_{N-1} = \prod_{j=1}^{N-1} S_j \tag{2.54}$$

However, according to the boundary conditions, $A_1 = 1$ and $B_N = 0$, so that A_N (denoted as C previously) is equal to:

$$A_N = \frac{1}{S_{11}} \tag{2.55}$$

given that

$$S_{TOT} = \begin{pmatrix} S_{11} & S_{12} \\ S_{21} & S_{22} \end{pmatrix} \tag{2.56}$$

Thus the transmission coefficient $\mathbf{T}(E)$ for a given energy E is:

$$\mathbf{T}(E) = \frac{k_N}{k_1} \frac{1}{|S_{11}|^2} = \frac{\sqrt{E - \phi(x_N)}}{\sqrt{E - \phi(x_1)}} \frac{1}{|S_{11}|^2} \tag{2.57}$$

The transmission coefficients for a Schottky barrier with different doping levels is plotted in figure 2.10 alongside the classical transmission coefficient for two different applied biases. There are two features that distinguish quantum mechanical transmission from classical transmission: The first, as mentioned above, is that even below the barrier height, there is a nonzero probability of transmission, referred to as quantum tunneling. For higher doping levels, the barrier is thinner and the probability of tunneling increases dramatically. At these doping levels, the leakage current will be substantially larger than what the classical model predicts.

The second feature is quantum reflection, which is that even for energies above the barrier height, there is a non-zero probability of reflection i.e. there is a probability less than 1 for transmission, whereas the classical model predicts perfect transmission for these energies. When the doping is low enough, there is little tunneling current, and the quantum model predicts a leakage current that is lower than

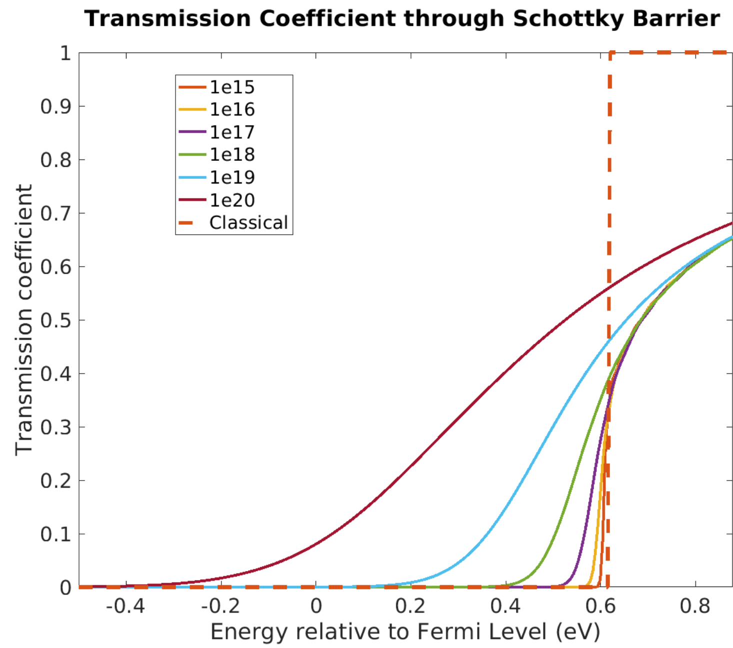

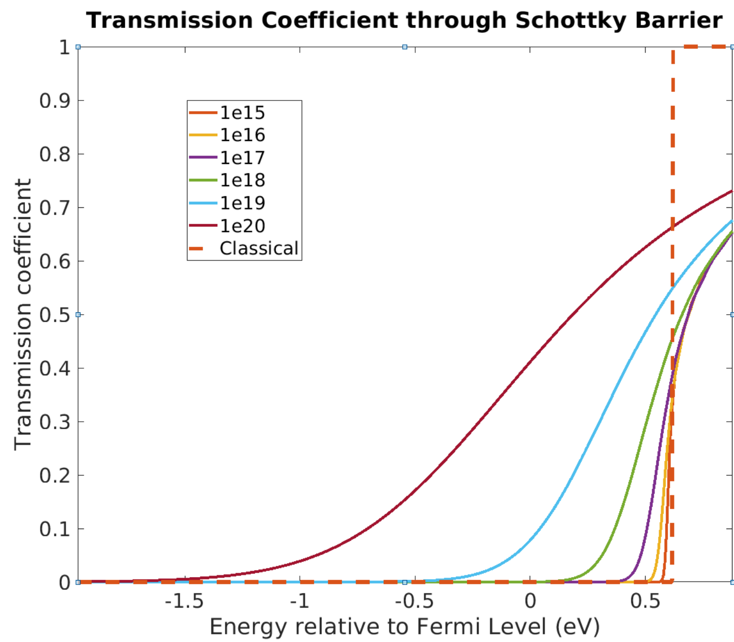

Figure 2.10: Transmission coefficient through 0.62 eV Schottky barrier with different donor doping levels for an applied reverse bias of (top) 0.6 V and (bottom) 10 V. The classical step function is also graphed in dashed line alongside to indicate barrier value

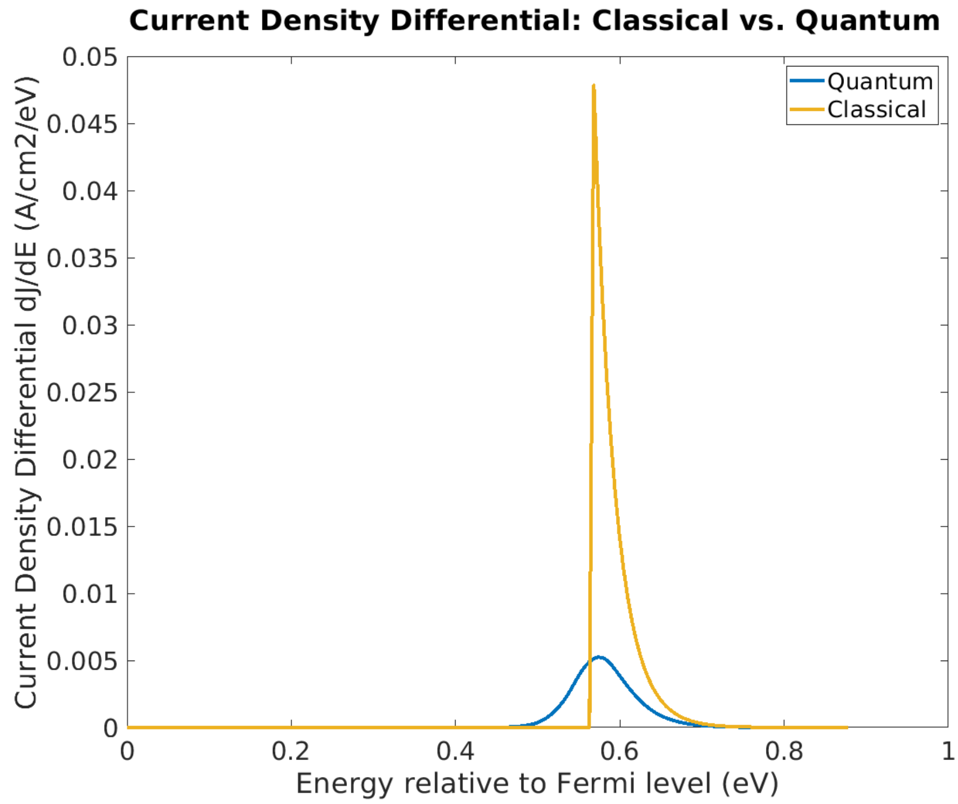

Figure 2.11: Differential current density through a 0.62 eV barrier for a doping concentration of 10^{16} cm^{-3} at an applied reverse bias of 0.6 V is calculated using the classical and quantum models. The reduction in current in the quantum model is due to quantum reflection.

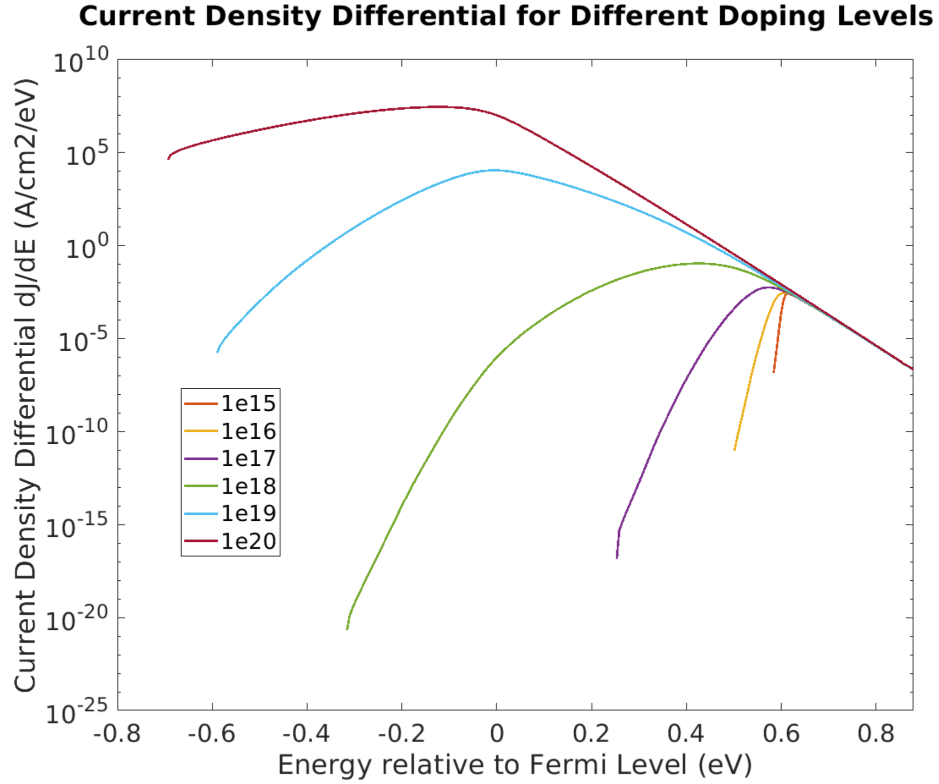

Figure 2.12: Differential current density through a 0.62 eV barrier calculated for different doping concentrations at an applied reverse bias of 10 V.

what the classical model predicts, due to quantum reflection. The differential current density through a 0.62 eV barrier for a doping concentration of 10^{16} cm^{-3} is plotted in figure 2.11, calculated using the classical model and the more accurate quantum model, highlighting the reduction of predicted current due to quantum reflection. This is an effect that cannot be captured with approximation schemes such as the Wentzel-Kramers-Brillouin (WKB) approximation, which predicts perfect transmission for energies above the barrier and will always overestimate the leakage current.

In figure 2.12 the differential current densities at different doping levels with

respect to energy is plotted on a log scale, for a given barrier height and applied bias. It is this curve that is integrated to give the current density. Note that for high energies, all curves fall off the same way, due to a drop in the electron population at those energies. For low energies, the curves fall off due to a drop in the transmission coefficients, which displays a large dependence on doping level. As shown, increasing doping levels lead to massive order of magnitude increases in current density. The total current densities for the different doping levels are then plotted in figure 2.13 with respect to applied bias for a given barrier height, alongside the respective classical prediction for each doping level. As mentioned earlier, the classical prediction overestimates the current for low doping levels and significantly underestimates the current for high doping levels. The variation among the classical models is due to IFBL.

2.2.2 Fermi Level Pinning

To correctly model the I-V characteristics of Schottky diodes, an accurate value of ϕ_{B0} must be used. The Schottky-Mott Rule states that [54]:

$$\phi_{B0} = \phi_M - \chi_S \tag{2.58}$$

where ϕ_M is the work function of the metal and χ_S is the electron affinity of the semiconductor, which measure the energy required to excite electrons (conduction electrons in the semiconductor case) to vacuum. Both parameters depend only on the material and should be independent of any geometries involved.

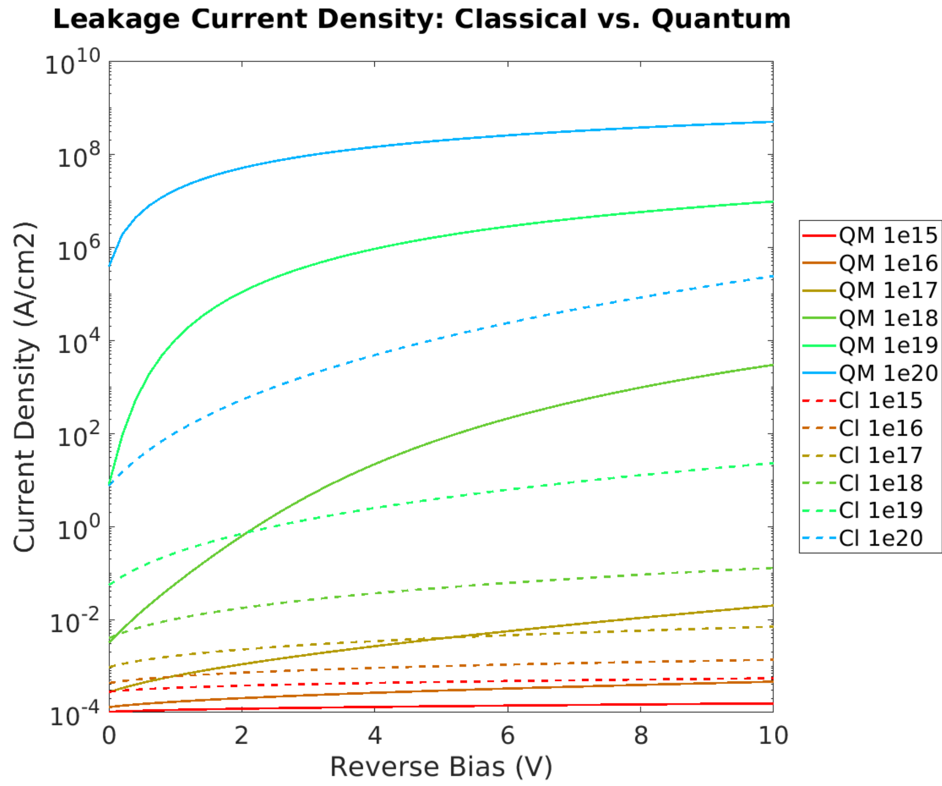

Figure 2.13: Current density through a 0.62 eV Barrier for different doping concentrations, with the quantum models (solid) plotted against the classical models (dashed) for comparison. The variation in the classical models is due to IFBL

However, in practice this ideal relationship is rarely seen, and in early devices, ϕ_{B0} was found to be largely independent of the metal involved. This effect was called 'Fermi Level Pinning' and is largely believed to be due to defects at the metal-semiconductor interface on the semiconductor side. A high enough concentration of defects will 'pin' the Fermi level to the energy level of the defects, independent of the metal. As fabrication techniques improved, the density of defects at the interface was reduced so that some dependence of ϕ_{B0} on ϕ_M occurred, modeled by the relationship:

$$\phi_{B0} = S(\phi_M - \chi_S) + C \tag{2.59}$$

Where S < 1 describes the strength of the dependence on the metals involved and C is a fitted constant. Previous studies have found values of S ranging between 0.2 and 0.7 [46] [47]. In order to correctly measure a value of S, each study must perform the same fabrication techniques on a variety of metals as to isolate the role of the defects (A study using one metal cannot determine a value for S, as at minimum two work functions are required to generate a slope). A study by Ewing et al. [48], found a value of S=0.45 when working with metals Ti, Ni, and Pt, and was able to attribute the pinning to local defect states at 0.62, 0.82, and 1.07 eV below the conduction band in 4H-SiC, and suggested these defect states were due to point defects and stacking faults intrinsic to 4H-SiC.

Additionally, the effect of the pinning was modeled as two diodes in parallel, one with a low barrier and one with a high barrier. The low barriers manifested

at low voltages and were found to be entirely independent of the metal involved, correlating directly to the defect states. The high barriers manifested at high voltages and it was these barriers that were found to have the S=0.45 relationship. The interpretation is that defect clusters locally pinned areas of the diode, so in these regions the barrier was equal to the defect energy, and at low voltages, all the current passed through the low barrier regions, whereas at higher voltages, not all the current could pass through these regions, and some electrons would conduct through the unpinned areas. Whereas some electrons 'saw' the ideal barrier height, others only experienced the pinned height, and so an effective barrier height was measured with an S=0.45 relationship. The I-V sweeps were only performed for forward bias, but from the results, one can infer that in reverse bias, the pinned low barrier will be significant, and so defects at the interface will greatly affect the reverse bias leakage current. Especially in the case for n-type 4H-SiC, these defects located near the conduction band will create difficulty in fabricating a large enough barrier to hold off the reverse bias leakage.

2.2.3 Theory vs. Experiment

Measurements on n-type 4H-SiC Schottky diodes with a doping concentration of 10^{16} cm^{-3} were carried out by Mitchell Gross, Aysanew Abate, Dr. Akin Akturk and Dr. Zeynep Dilli [55], and the results were compared to the theoretical models generated by the tunneling current calculation. The results are graphed in figure 2.14 on a log scale alongside the theoretical curves calculated at the same doping

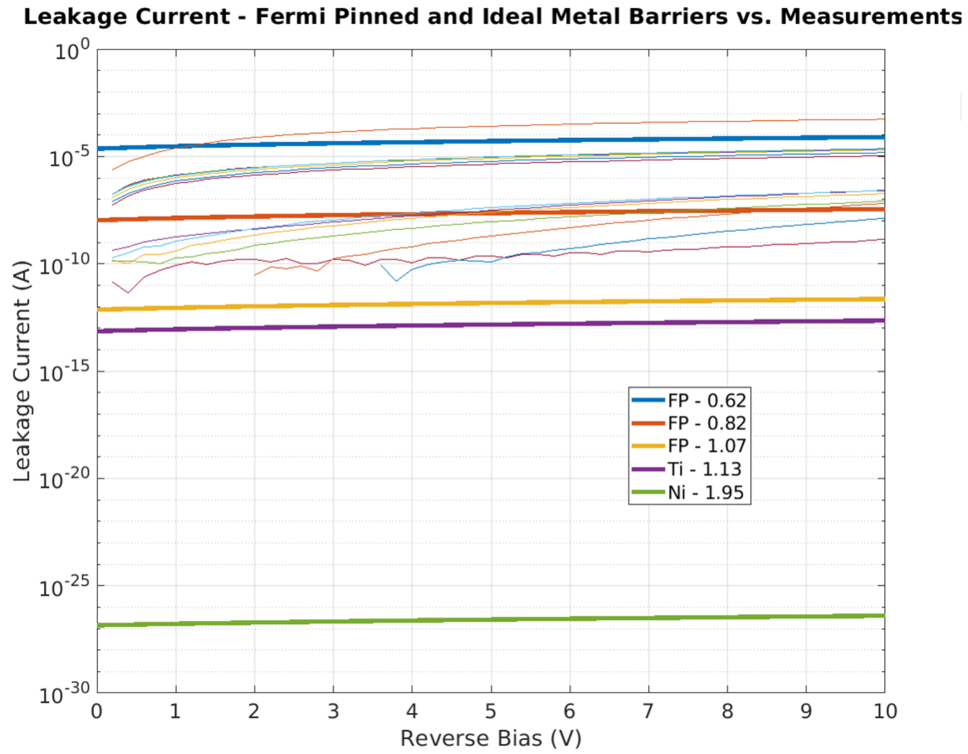

Figure 2.14: Measured leakage current through Ti on n-type 4H-SiC Schottky barrier is graphed for different diodes in the unbolded curves. Bolded curves are from theoretical calculations using a doping concentration of 10^{16} cm^{-3}, using Fermi pinned barriers equal to the respective defect energy and for two ideal metal barriers, Ti and Ni.

concentration for various barrier heights: the three defect barriers found by Ewing et al. [48] i.e 0.62,0.82 and 1.07 eV, and the ideal barrier for Ti (1.13 eV) and Ni (1.95 eV). From the comparison, it is clear that Fermi pinning is likely the reason for the large leakage currents seen, as the measured values fall within the order of magnitude range of the Fermi pinned calculations.

According to Ewing et al., it is suggested that the Fermi pinning occurred from defect clusters, as only a portion of the diodes measured displayed the nonideal behavior, i.e. it was these diodes where the clusters were present. Among diodes with a diameter of 500 μm, 15% displayed non-ideal behavior, and among diodes with a diameter of 300 μm, 7% displayed non-ideal behavior. This is consistent with the theory that the clusters are uniformly distributed: if there is a probability p_1 of finding a cluster in an area A_1, and the clusters follow a uniform distribution, then the probability p_2 of finding a cluster in an area A_2 is:

$$p_2 = 1 - (1 - p_1)^{\frac{A_2}{A_1}} \tag{2.60}$$

Plugging in the above values yields:

$$1 - (1 - 0.07)^{\frac{250^2 \pi \mu m^2}{150^2 \pi \mu m^2}} = 0.183 \tag{2.61}$$

which is quite close to the reported 15%. The measured diodes reported here had an area of 5.76 mm^2. Plugging into the above formula yields:

$$1 - (1 - 0.07)^{\frac{5.76 mm^2}{150^2 \pi \mu m^2}} = 0.997 \tag{2.62}$$

Essentially, a diode with such an area will almost always experience Fermi pinning due to defect clusters, which is consistent with the results graphed above.

2.2.3.1 Effective Doping Level

While the order of magnitude of the measured currents is consistent with the calculated Fermi pinned currents, the overall bias dependence of the measured values is stronger than the theoretical prediction for a doping of 10^{16} cm^{-3}. However, when compared with other doping level current calculations, the measured values appear to have a bias dependence between that of 10^{16} cm^{-3} and 10^{17} cm^{-3}, suggesting the actual barrier is effectively thinner than would be due to the reported doping concentration alone. This could likely be due to defects present in the depletion region, which could be causing barrier thinning as well as trap-assisted tunneling.

The measured values, as seen in figure 2.14, are broken into two groups according to order of magnitude, and are likely due to two different defects being the dominant set of clusters. When compared to higher doping concentrations to match bias dependence, different doping levels were found to match for the two different groups.

The calculated current was compared to the measured values for different doping levels and the average error between the theoretical and measured values was calculated and graphed in figure 2.15 for the higher and lower current groups. Since it is the bias dependence that is being matched here and not the absolute value of current, each calculated curve was scaled down so that the current at the highest

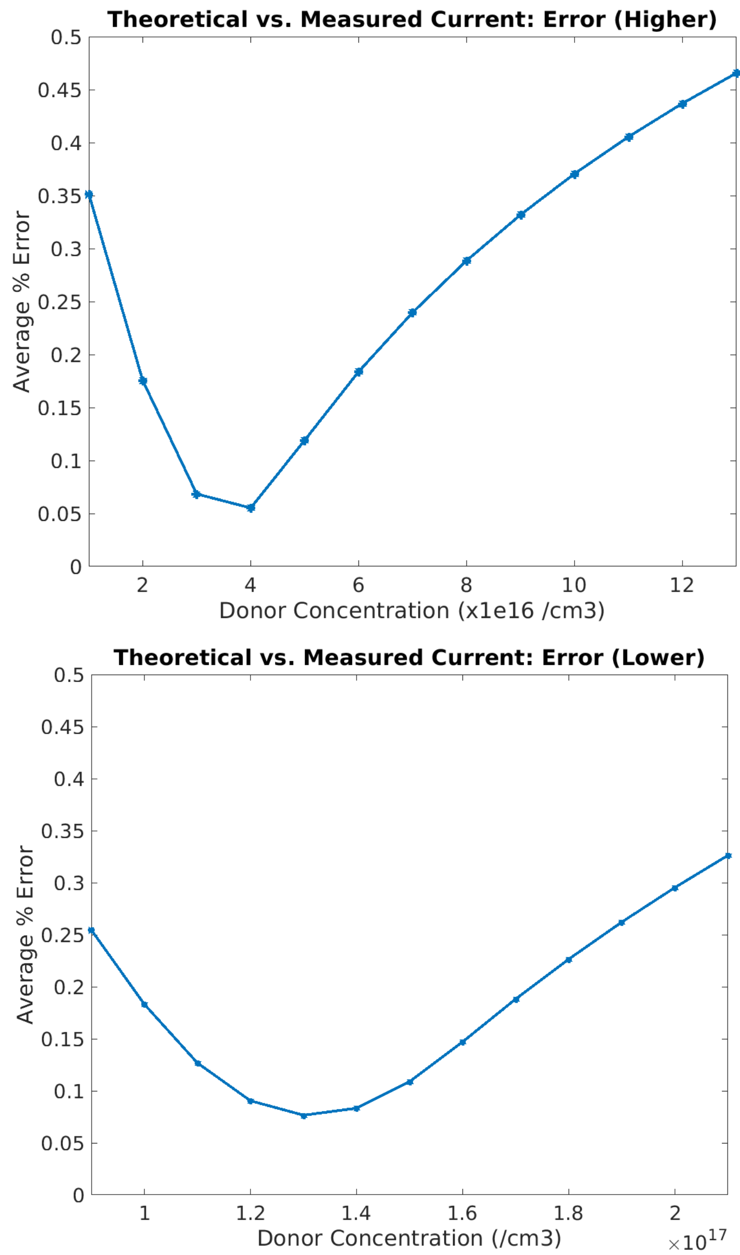

Figure 2.15: Average error between theoretical currents for different doping levels and measured current in the (top) higher current group and (bottom) lower current group

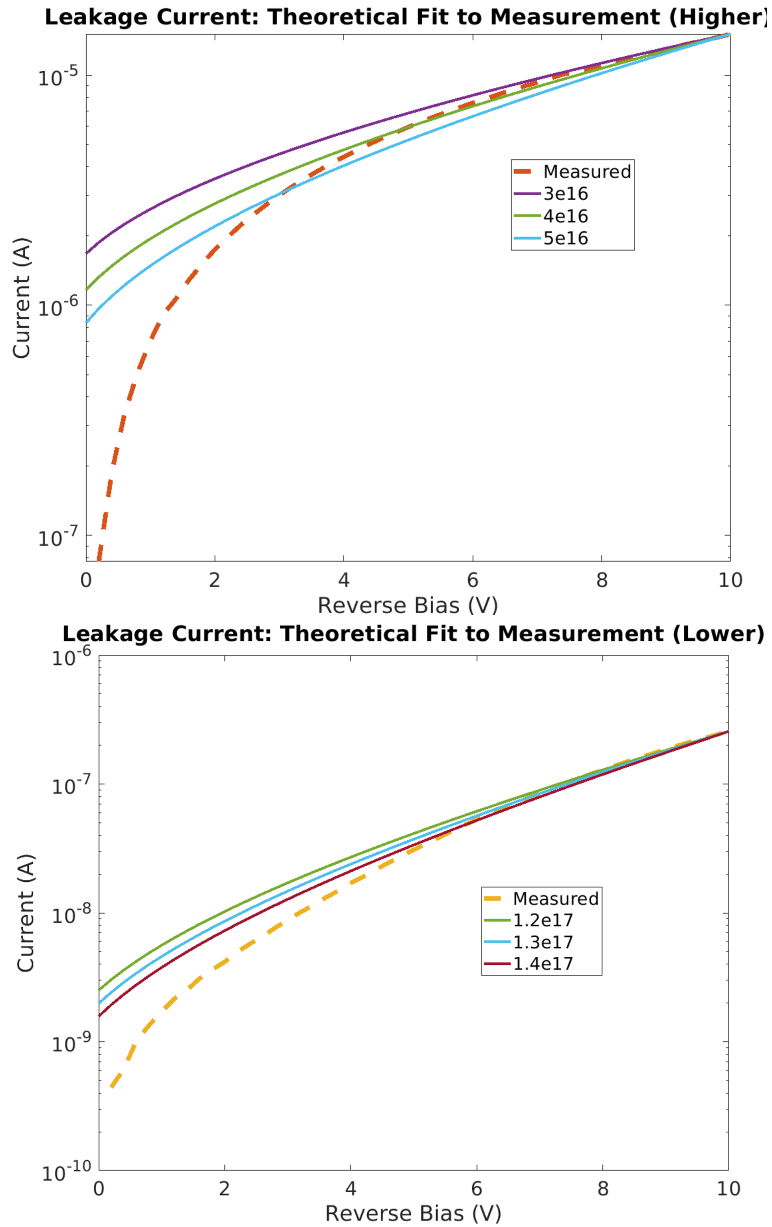

Figure 2.16: Best fit theoretical current curves graphed alongside a measured curve from the (top) higher and (bottom) lower current groups. For each comparison, the three best fit doping levels were used.

bias was set equal. The physical justification for this is that the presence of the clusters create an effective area that the pinned current actually flows through [45], with the effective fraction equal to the ratio between the measured currents and the best fit calculation. From the graph, for the higher current group, the minimum error was achieved for a doping concentration between 3x10^{16} and 5x10^{17} cm^{-3}, with a minimum average error of about 5.5%. For the lower current group, the minimum error was achieved for a doping concentration between 1.2x10^{17} and 1.4x10^{17} cm^{-3}, with a minimum average error of about 7.7%. The average effective fraction of the areas are 4.6% and 5.0%, for the higher and lower groups respectively, compared to a fractional area value of 1.1% found by Li et al., [45] on Ni/4H-SiC diodes at 363 K with a donor concentration of 5x10^{15} cm^{-3}. However, that fractional area value was found by matching experimental measurements to a classical formula. From the above theoretical analysis, at that given doping level of 5x10^{15} cm^{-3}, quantum reflection would cause the classical formula to overestimate the current by a factor of approximately 3. Accounting for this, the fractional area would then be about 3.3%. That there is such strong agreement between studies is a good indication that the effective doping concentration and barrier width, and subsequent area fraction, is accurate. The theoretical curves for the best fit doping levels are graphed alongside one of measured curves from the corresponding group in figure 2.16. While the theoretical curves have similar slopes for the larger bias values, for low biases, the measured values drop off much quicker. This could be due to a consequence of the trap-assisted tunneling: According to Dolny et al., [42] the emission rate for trap assisted current will have a linear field dependence that dominates the other field

dependent terms at low biases.

2.3 Future Research

For the future, trap-assisted tunneling and barrier thinning must be more accurately modeled. The relevant traps and their effective energies and concentrations will need to be determined, and the correct form of trap assisted tunneling will need to be included.

Methods to possibly passivate the traps or reduce the surface states to alleviate Fermi pinning will need to be considered in order to reduce the leakage current

Chapter 3: High Mobility MOSFETs: Germanium

3.1 Background Overview

3.1.1 Basic Properties of Germanium

3.1.1.1 Crystal Structure

Ge, like Si, is a group IV semiconductor, and the two share many properties. Both form diamond FCC crystal lattices with similar lattice constants, 5.43 A for Si and 5.66 A for Ge. Due to the similar lattice constants, Ge can be integrated unto Si surfaces. It is still no trivial matter to do so, as the small difference in bond lengths can still generate a high density of lattice mismatches. Sometimes SiGe hybrids are employed to work through this or thin layers of Ge are deposited, which will strain the lattices but won't generate as many mismatches. Straining Ge and Si has several advantages, such as reducing effective carrier masses to increase mobility.

3.1.1.2 Electrical Properties

Ge and Si both have indirect bandgaps, with 0.66 eV for Ge and 1.1 eV for Si, with both energies corresponding to the infrared regime. Descending the group IV

column, the materials become more metallic with weaker bonds, going from the very brittle extreme of carbon to the very soft extreme of lead. As expected, Ge forms weaker bonds than Si, which causes it to be more reactive and more temperature sensitive, with a melting point of 1210 K as opposed to 1685 K for Si. Being more reactive and temperature sensitive makes Ge more problematic during fabrication, requiring low temperature procedures and more robust passivation techniques.

The advantage of Ge over Si lies in its lower effective carrier mass. Band structure analysis reveals that for most semiconductors, a lower bandgap corresponds to a lower effective mass [56]. As expected, the conductivity effective electron mass in Ge is 0.117 m_0 vs. 0.260 m_0 in Si, and the effective hole masses in Ge are 0.33 m_0 and 0.043 m_0 (heavy and light, respectively) vs. 0.49 m_0 and 0.16 m_0 in Si, where m_0 is the rest mass of a free electron. The result is that Ge offers a higher carrier mobility, with potentially over two-fold improvement to electron mobility and four-fold improvement to hole mobility. This makes Ge ideal for low voltage high speed circuitry e.g. CMOS devices. Additionally, since the ratio of mobilities between electrons and holes is smaller for Ge than it is for Si, Ge CMOS devices will use available chip space more efficiently than Si CMOS devices.

3.1.2 Oxide/Semiconductor Interfaces

Another similarity between Si and Ge is both have a native thermal oxide, SiO_2 and GeO_2 respectively. This makes Ge a very attractive candidate for CMOS technology, since thermal oxides can typically be fabricated with a significantly

lower interface defect density than other oxides, such as deposited oxides. The operating current for MOSFETs exists in a channel right at the oxide/semiconductor interface, and the conductivity of the channel is heavily dependent on the quality of the interface. Thus major improvements to the performance of MOSFETs is possible by improving the quality of the interface. Just as Si and Ge share many properties, so do SiO_2 and GeO_2. Both exhibit amorphous and crystalline phases, with the crystalline phase forming an α-quartz structure. Both oxides have the same stoichiometry, with each semimetal atom bonded to 4 oxygens, which are each bonded to 2 semimetals. Both oxides can be fabricated via thermal oxidation of the corresponding substrate. As mentioned above, Ge is more temperature sensitive, and so thermal oxidation is conducted at a lower temperature than it is for Si. Additionally, the oxidation mechanism for GeO_2 growth differs from SiO_2 growth.

3.1.2.1 Si/SiO_2 Interface Structure

Si oxidation occurs via interstitial oxygen molecules diffusing through the oxide network and reacting with Si at the interface. The seminal Deal-Grove model [14] models this growth quite accurately. The interface that forms is very abrupt, ideal for channel conductivity, due to the energetics of Si-O bonding. As Si atoms transition from being completely bonded to other Si atoms in the substrate to being completely bonded to O atoms in the oxide, the Si atoms exist in intermediate oxidation states i.e. being bonded to one to three O atoms. These intermediate oxidation states require additional energy to form, by as much as 0.5 eV per O

atom [2], making them unfavorable compared to the fully oxidized states. Thus the total volume of partially oxidized Si atoms is minimized i.e. made flat and narrow, making an abrupt interface the most favorable configuration.

3.1.2.2 Ge/GeO_2 Interface Structure

Ge oxidation is a more complicated process and cannot be simply modeled with a Deal-Grove like model. Ge oxidation occurs via oxygen atoms bond hoping through the network. An oxygen atom incorporates itself into the oxide network via the formation of a peroxyl configuration, where two oxygen atoms are bonded to each other between two Ge atoms, depicted in Fig.3.1. Then one of the two oxygen atoms will break away to form a new peroxyl configuration in a neighboring region of the network. In this way oxygen atoms are transported through the oxide network to the interface [15]. Unlike in the case for Si, the resulting interface is not abrupt and instead a substoichiometric region of GeO_x forms, where x is less than 2. This reflects the energetics of Ge-O bonding, where unlike with Si, there is not much additional energy required to form intermediate oxidation states, requiring only around 0.1 eV additional energy per O atom [2]. Thus there is little energy incentive to minimize the volume of the intermediate region. One of the main reasons for these differences between Si oxidation and Ge oxidation is that Ge forms weaker and more flexible bonds with O than Si does (include bond energy and angle variations). This makes forming intermediate oxidation states and peroxyl states more energetically favorable, as there is less cost in breaking and forming bonds

as well as rearranging the network to accommodate strain. Additionally, the extra flexibility of Ge-O bonds allows for tighter angles to form in the network, which results in differences in the ring statistics between the two oxides [15]. In particular, there is a higher density of low order rings in GeO_2 (3- or 4-rings) than in SiO_2, which increases the energy barrier for O_2 interstitial diffusion (as the rings are the regions O_2 must pass through to migrate between interstitials). This additional factor contributes to Ge oxidation favoring peroxyl diffusion over O_2 interstitial diffusion.

3.1.2.3 Volatility of Ge/GeO_2 interface

To further complicate the fabrication process, the Ge substrate reacts with the oxide layer in ways that do not occur for Si. GeO_2 has been observed to be volatile at temperatures exceeding 400 C, by desorbing as GeO gas [5] [6]. Previous isotope tracing experiments revealed that the production of GeO is due to the formation of oxygen vacancy defects at the Ge/GeO_2 interface [7]. The experiments suggests that oxygen atoms by the interface will hop over into the substrate, leaving behind an oxygen vacancy i.e. Ge-Ge bond inside GeO_2. It is this reaction that leads to the formation of the substoichiometric intermediate region discussed previously, with oxygen atoms diffusing into the substrate via bond hopping. The vacancy inside the oxide will then diffuse, also via a bond hopping process, where neighboring oxygen atoms will hop to fill the vacancy, leaving behind another one. If a vacancy migrates to the top of the oxide, it will alter the surface configuration and make it favorable for

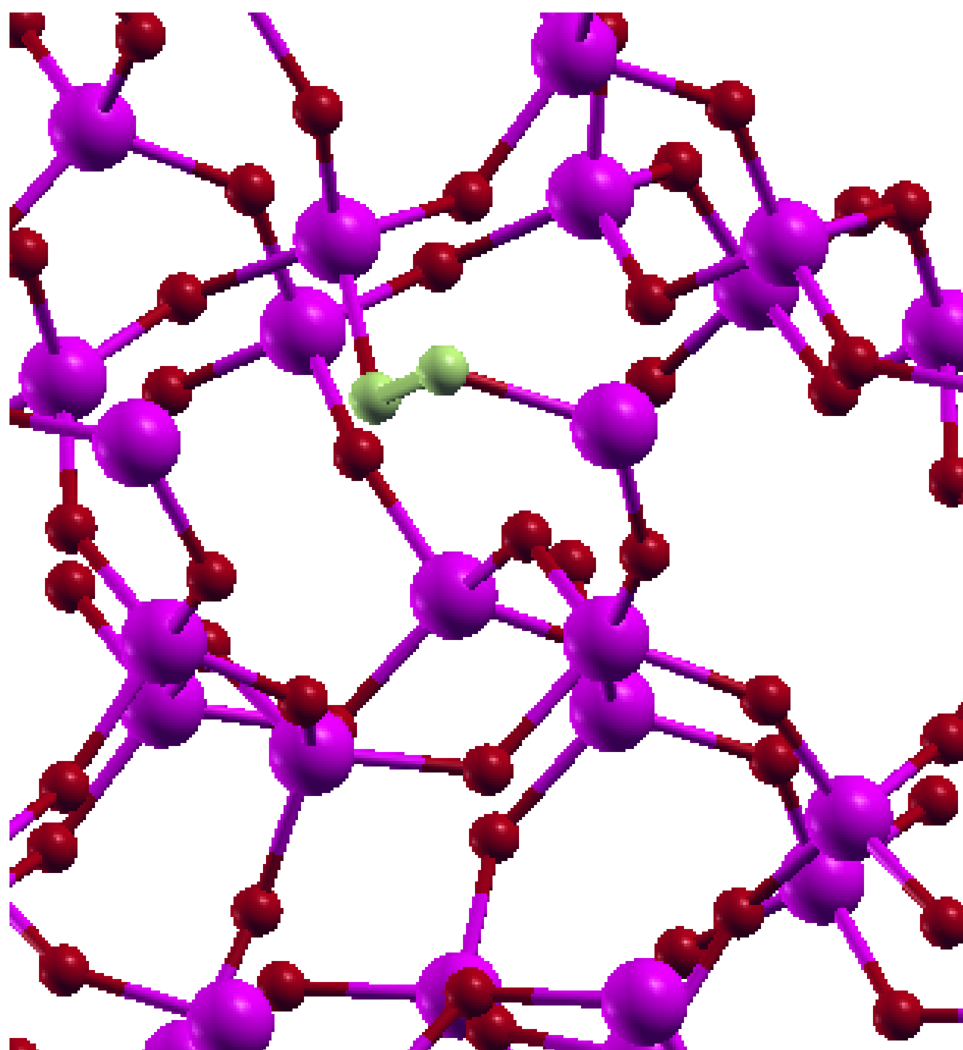

Figure 3.1: Section of 73 atom supercell of amorphous GeO_2 with a peroxyl defect. Peroxyl O atoms are highlighted in green, Ge atoms in purple, regular O atoms labeled in red.

a GeO molecule to break off and desorb [6]. At high enough temperatures, enough vacancies form at the interface and are able to migrate quickly enough to the surface to make the GeO desorption substantial. Thus low temperature operation is critical for Ge wafer fabrication.

3.1.2.4 Interface Defects

Understanding oxygen vacancies in the Ge/GeO_2 system is critical to understanding ways to improve the interface and oxide quality. Oxygen vacancies are responsible for GeO desorption and for the formation of an intermediate oxide region [4] [7], as well as charge trapping and the formation of another type of defect called Valence Alternating Pairs (VAPs) [2]. VAPs form by the splitting of the Ge-Ge bond, where one Ge atom picks up a negative charge while the other bonds to an O atom, making it triply coordinated and positively charged. A high density of VAPs leads to a high amount of trapped charge by the interface, which will alter the threshold voltage, as well as reduce the band offset between the substrate and oxide, leading to higher oxide leakage. Understanding how to passivate oxygen vacancies and VAPs is therefore crucial to forming high quality Ge/GeO_2 interfaces.

3.1.3 Density Functional Theory

3.1.3.1 Motivation

Understanding the atomic structures of the defects is crucial towards understanding how to passivate them and reduce their effects in order to fabricate high

quality devices. In order to understand and characterize the various atomic configurations relevant to this research, the effects of quantum mechanics must be incorporated, which ultimately requires solving the Many-Body Schrodinger Equation, shown below:

$$E\Psi(r_1, ..., r_N, R_1, ..., R_M) = H\Psi \tag{3.1}$$

where

$$H = -\sum_{r_i} \frac{\hbar^2}{2m}\nabla_i^2 - \sum_{R_j} \frac{\hbar^2}{2M_j}\nabla_j^2 - \sum_{r_i}\sum_{R_j} \frac{Z_j q^2}{4\pi\epsilon_0|r_i - R_j|} + \frac{1}{2}\sum_{r_i}\sum_{r_j} \frac{q^2}{4\pi\epsilon_0|r_i - r_j|} + \frac{1}{2}\sum_{R_i}\sum_{R_j} \frac{Z_i Z_j q^2}{4\pi\epsilon_0|R_i - R_j|} \tag{3.2}$$

E is the energy of the atomic configuration, H is the Hamiltonian and Ψ is the wavefunction of N electrons with mass m and M atomic nuclei with mass M_j and charge Z_j. The first two r.h.s terms are the kinetic energy terms of the electrons and atomic nuclei, respectively, and the last three terms are the electrostatic potential energy terms of the electron-nuclei attraction, the electron-electron repulsion, and the nuclei-nuclei repulsion.

Solving the Many-Body Schrodinger Equation becomes increasingly more and more difficult as the number of particles increases, and is virtually impossible for the atomic configurations usually under consideration. Rather than consider the

all-electron wavefunction, the electron density is calculated and Density Functional Theory (DFT) is applied. DFT reframes the problem by focusing on the electron density, defined as:

$$\rho(r) = N \int ... \int |\Psi(r_1, .., r_{N-1}, r)|^2 d^3r_1...d^3r_{N-1} \tag{3.3}$$

The electron density is a function of a single position, unlike the wavefunction, and thus turns the problem into a tractable one

3.1.3.2 Kohn-Sham Equations

In order to minimize the (approximate) energy functional, Kohn and Sham [17] expressed the electron density in terms of a wavefunction composed of non-interacting electrons, so that the density can be rewritten as a sum over the probability density functions of the non-interacting electron orbitals

$$\rho = \sum_{i=1}^{N} |\phi_i|^2 \tag{3.4}$$

Using the fact that the integral of the density over all space must equal N (the number of electrons) as a constraint, the energy functional minimization is reframed into a Lagrange multiplier problem, yielding N decoupled equations called the Kohn-Sham Equations:

$$\epsilon_i \phi_i = \frac{-\hbar^2}{2m} \nabla^2 \phi_i + V_{KS} \phi_i \tag{3.5}$$

ϵ_i is the lagrange multiplier and approximately equals the ionization energy

for the ith (although this usually only holds for the highest energy orbital). V_{KS} is the Kohn-Sham potential and represents the potential one electron sees when the rest of the electrons have been ”smeared” out.

The equations can be solved self-consistently by using the density to generate the Kohn-Sham potential, which in turn is used to solve for the electron orbitals, which are then used to calculate the density, and these steps iterate through until the change in the density is small.

3.1.3.3 Application of DFT

To apply DFT numerically, the open-source Quantum ESPRESSO suite [57] was utilized. In order to apply DFT numerically on the computer, a number of additional approximations and considerations need to be included. Due to the nature of most of the solid state systems under consideration, the DFT calculations are carried out over periodic unit cells with periodic boundary conditions. Appropriately, all relevant functions e.g. the electron density, the potential energy, are expressed in a plane wave basis, where each basis vector comes from a different Brillouin zone i.e. from a different G-vector. For practical purposes, only a finite basis set can be implemented, and so a cut off for the basis is specified in terms of the maximum energy of the plane wave given by:

$$E_{max} = \frac{\hbar^2}{2m}(\frac{2\pi}{\lambda_{min}})^2 \tag{3.6}$$

The cut off is usually chosen so that the minimum wavelength, λ_{min}, is on

the order of, if not smaller than, the typical chemical bond lengths in the atomic configuration in question. Typical cut off values of 400 to 900 eV are chosen, corresponding to lengths close to half an angstrom. Including a larger cut off for the basis places a larger burden on the required RAM usage, and for computationally practical reasons, simulations are initially executed using a reduced energy cutoff. Once the simulation has finished running, additional simulations are executed with progressively increasing energy cut off until the final calculated result converges with all subsequent simulations.

All other details involved in the mathematics of the DFT calculation are described in Appendix A. A flowchart of the algorithm is depicted in Fig.3.2.

3.2 Current Research

My current research focuses on applying DFT to various atomic configurations to investigate how different fabrication techniques will affect device performance. Specifically, the Ge/GeO_2 interface is investigated, along with related crystal structures and defects. In addition, various defect passivation techniques as well as other related configurations were investigated. The goal of the research is to not only provide a qualitative understanding of the Ge/GeO_2 interface and related defects, but also to provide a quantitative understanding of the various fabrication parameters that need to be tuned in order to generate high quality semiconductor devices.

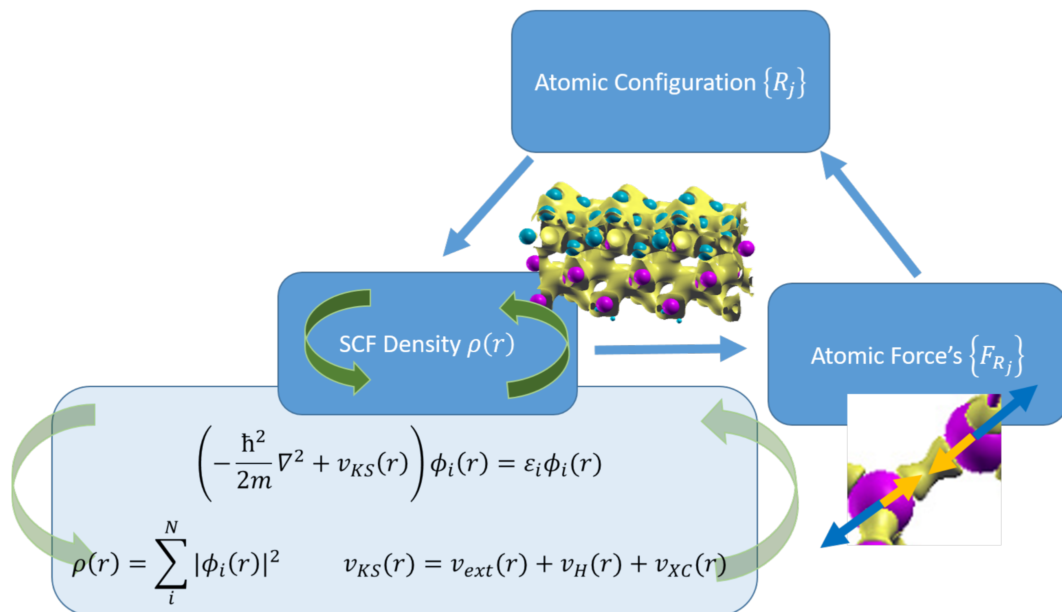

Figure 3.2: Flowchart depicting the three main steps in the DFT calculation: The atomic coordinates are used to generate the electron density via a nested self-consistent loop that utilizes the Kohn-Sham equations and effective Kohn-Sham potential v_{KS}. The density is used to calculate the atomic forces via the Hellman-Feynman theorem [57]. The atomic forces are then applied to each atom to find the change in the coordinates. The algorithm loop follows the logic of the Born-Oppenheimer approximation, where the change in the electron density and change in atomic coordinates can happen separately, as the electrons respond to changes in the atomic coordinates over a much smaller time scale.

3.2.1 DFT Simulations of Bulk Supercells: Ge, GeO_2, and Ge/GeO_2 interface

In order to use DFT to investigate defect structures and chemical reactions in Ge and GeO_2, baseline supercell structures need to be constructed first in order to calibrate results and ensure accuracy. Many-atom supercells of bulk materials and surface structures were constructed and relaxed using DFT, before being modified to include defect structures and/or relevant chemical reactions. This allows for the formation energy of the defect structures to be calculated using the following formula:

$$E_f[X] = E_{tot}[X] - E_{tot}[bulk] - \Sigma n_i \mu_i + qE_F \quad (3.7)$$

Where X represents the supercell with the defect, E_f is the formation energy, E_{tot} is the total calculated energy of the supercell, n_i is the change in the number of atoms of type i when transforming from the bulk structure to X, and μ_i is the chemical potential of atoms of type i. If the defect or impurity in X in charged, then the last term has to be included, where q is the charge of defect, and E_F is the Fermi level, defined with respect to the valence band maximum of the bulk supercell.

The initial bulk supercell DFT calculations are therefore used to compute the second and third terms in the formation energy formula, as the chemical potentials can often times be calculated using the bulk structures. A critical detail when carrying out these calculations is to only compare energy calculations from simulations with congruent input parameters i.e. Basis energy cutoff, k-space gridpoints, energy

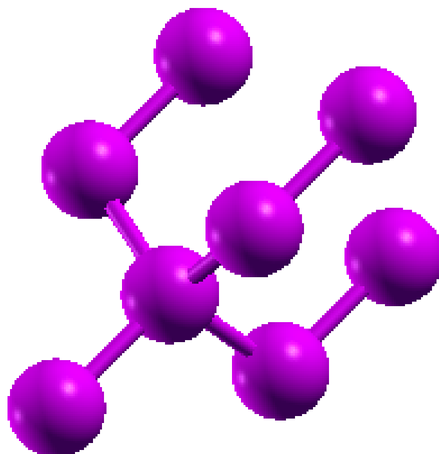

Figure 3.3: 8 atom FCC unit cell of bulk Ge.

convergence threshold, and force convergence threshold.

3.2.1.1 Bulk *Ge*

Bulk *Ge* was constructed using an 8 atom FCC unit cell. The unit cell is shown in Fig.3.3. An energy cut off of 400 eV was set and a 2x2x2 kpoint grid was used. Convergence was achieved when all force components were below 0.05 eV/Å. An scf simulation was then run using a hybrid functional using a 2x2x2 qpoint grid and increasing Brillouin zone sampling to reproduce the correct band gap. The resulting density of states is plotted in Fig.3.4. A final value for the bandgap of 0.615 eV was found, with all values plotted in Fig.3.5.

For surface reaction considerations, a *Ge* substrate surface was constructed using an 18 atom unit cell shown in Fig.3.6. Due to the periodic nature of the boundary conditions, the unit cell must be extended in the direction normal to

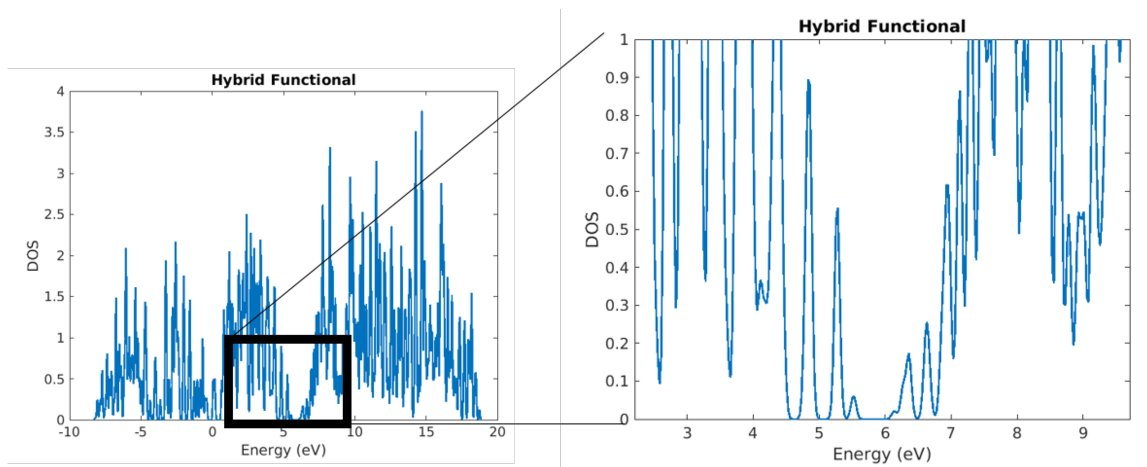

Figure 3.4: Density of States (DOS) plot of Ge using a hybrid functional to reproduce the correct band gap.

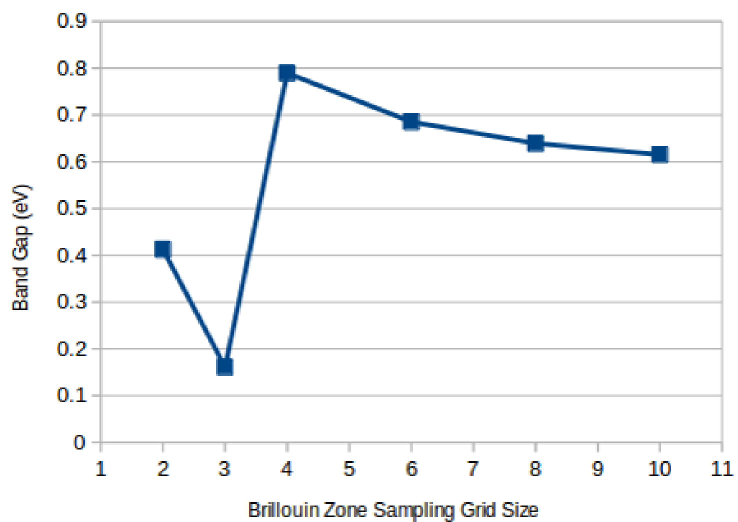

Figure 3.5: Calculated band gap of Ge with increasing Brillouin zone sampling size. Sampling size was increased by incrementally increasing the dimensions of the mesh grid.

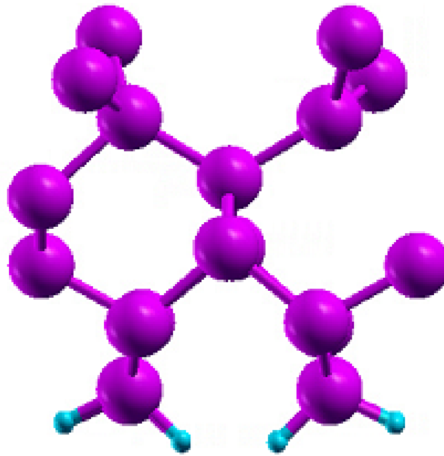

Figure 3.6: 18 atom unit cell used to simulate Ge substrate surface. Hydrogen atoms are included to satisfy the dangling bonds on the final layer. Positions of H atoms are held fixed during relaxation to simulate bulk.

the surface to create a layer of vacuum between the surface and the next periodic construction. This reduces the magnitude of the interactions between copies of the supercell along the surface normal. The structure was relaxed using an energy cut off of 400 eV and using the Gamma point to sample k-space. Convergence was achieved when all force components were below 0.05 eV/Å.

The Ge surface reconstruction produces an alternating pattern of asymmetric dimer pairs, detailed in Fig.3.7. To reduce strain, the dimer pairs buckle and charge is transfered from one member to the other. The positively charged Ge atom rehybridizes and forms 3 sp^2 σ bonds, which lowers the Ge atom and flattens the bonds into a planar structure. The negatively charged Ge atom fills its dangling sp^3 orbital, and is raised as the remaining 3 sp^3 σ bonds pucker. The charge localization for the dimer structure is depicted in Fig.3.8 where the transfer of charge is clearly

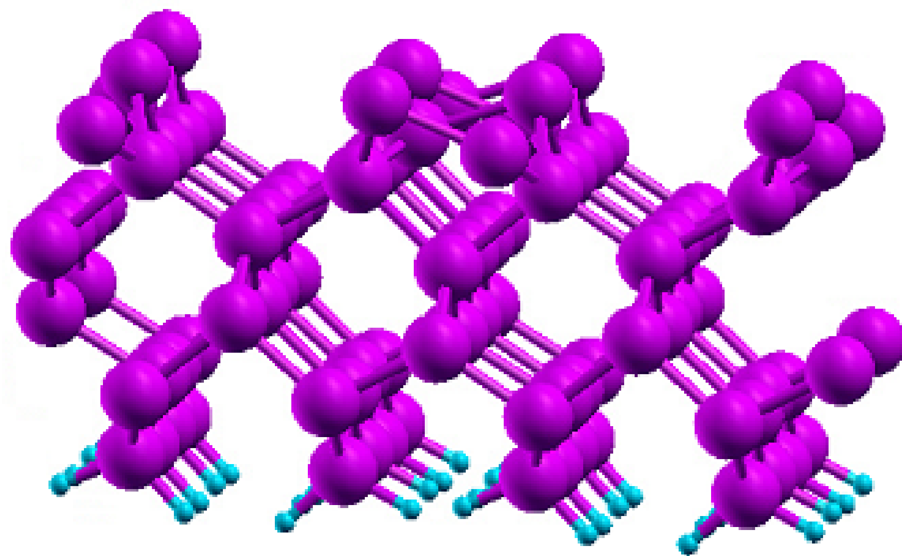

Figure 3.7: Supercell of multiple copies of surface unit cell. The dimer structures are clearly visible, forming rows with channels in between. The buckling of the dimers is seen to alternate parity progressing down the row.

indicated.

3.2.1.2 Bulk GeO_2

Crystalline GeO_2: Bulk crystalline GeO_2 was constructed using a 9 atom unit cell, shown in Fig.3.9. The structure was relaxed using an energy cut off of 400 eV and using the Gamma point to sample k-space. Convergence was achieved when all force components were below 0.05 eV/Å. The calculated results were compared to values from the literature, shown in table 3.1. As is evident, the calculated structure accurately predicts physical parameters.

Amorphous GeO_2: The next step was to use the crystalline form of GeO_2 to construct the amorphous form. Because GeO_2 is being investigated for its role in

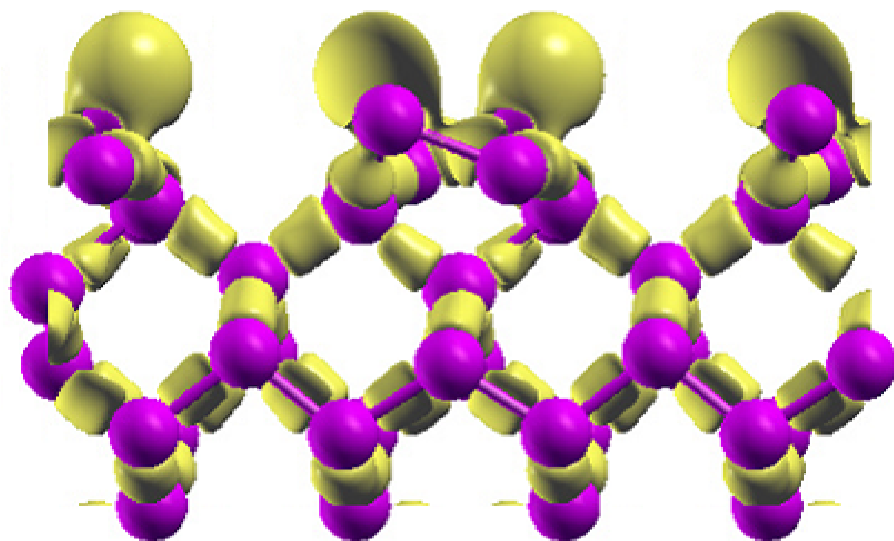

Figure 3.8: Isosurface Electron Localization Function (ELF) plotted on supercell of surface dimers. Isosurface is of an ELF of 0.8. The ELF indicates the localization of charge. Ge atoms are labeled with purple. Isosurface is labeled with yellow. The isosurface between atoms represents localization due to bonds. The large protrusion at the surface represents the completed sp^3 orbitals.

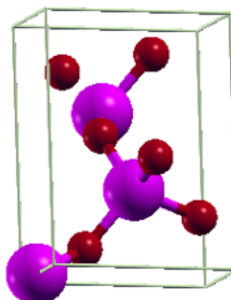

Figure 3.9: 9 atom unit cell of GeO_2 in the α-quartz polytype. Ge atoms are labeled with purple and O atoms are labeled with red.

Value	Calc.	Exp.
Formation Energy (eV)	4.813	4.84
Bond Length (Å)	1.77	1.74
Dielectric constant	2.97	3.01

Table 3.1: Comparison of calculated values to experimental values for GeO_2 α-quartz

MOSFET performance, the amorphous form of GeO_2 is of interest since that is the form of GeO_2 present in MOSFETs. The amorphous structure was formed using the Sequential Back Bond (SBB) method introduced by Ettisserry [26]. First the initial 9 atom unit cell of the crystalline GeO_2 was replicated to form a 72 atom supercell of crystalline GeO_2. Since the supercell represents a periodic structure, the supercell must be large enough in order to replicate the properties of a truly amorphous structure.

The SBB method was applied by first selecting a Ge atom, and flipping it across the plane defined by three of the O atoms it was bonded to, "puckering" the Ge atom. The "puckered" Ge atom is then bonded to another O atom, making it triply coordinated. One of the two Ge atoms initially bonded to the triply coordinated O atom is then "puckered" so that it breaks away from the respective O atom, and the process repeats until all the bonds are satisfied again.

Once all the bonds are satisfied, the new altered structure is relaxed and the process iterates a few more times through until the structure is appropriately amorphous. One of the resulting 72 atom amorphous supercells is shown in Fig.3.10. The SBB method reproduces an amorphous structure since the "puckered" configuration is related to a defect that naturally forms in the oxide, and thus the SBB iterations mimic the processes that occur at high temperature when a lot of defects form and

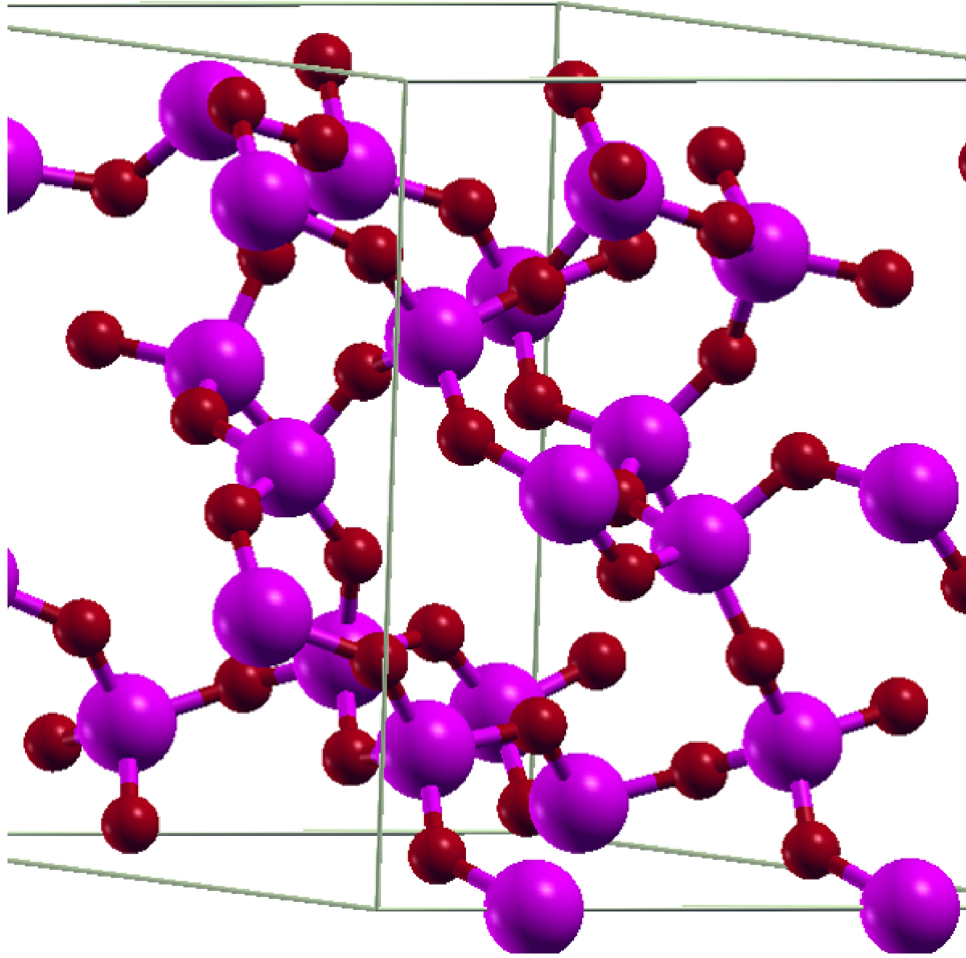

Figure 3.10: 72 atom supercell of amorphous GeO_2 formed by applying SBB method with 3 passes to a 72 atom supercell of α-quartz GeO_2. Ge atoms are labeled with purple and O atoms are labeled with red.

migrate through the oxide, altering the final configuration. The SBB method has the benefit of being less time consuming and less computationally draining than implementing melt and quench using molecular dynamics.

3.2.2 DFT Simulations of Defects and Passivation

3.2.2.1 Oxygen Vacancy

One of the primary defects of interest in GeO_2 in this research is the oxygen vacancy. Oxygen vacancies were studied by removing an oxygen atom from one of the 72 atom amorphous GeO_2 supercells and relaxing the structure. The structures were relaxed using an energy cut off of 900 eV and using the Gamma point to sample k-space. Convergence was achieved when all force components were below 0.05 eV/Å. One of the relaxed supercells with an oxygen vacancy is shown in Fig.3.11.

One of the main issues with oxygen vacancies is their ability to migrate and diffuse through the oxide during fabrication. Oxygen vacancies migrate by oxygen atoms "hopping" from neighboring sites. The reaction pathway for this migration reaction was calculated using an NEB [57]. To set up the NEB, some preliminary structures were relaxed first.

The initial and final configurations for the reaction pathway were derived from two different oxygen vacancy-containing supercells that were constructed from the same 72 atom amorphous GeO_2 supercell. In order to reduce computational demand, as well as reduce the effect of self-interaction between supercells, many of the atoms in the supercells were held fixed during the calculation. Only the hopping O atom,

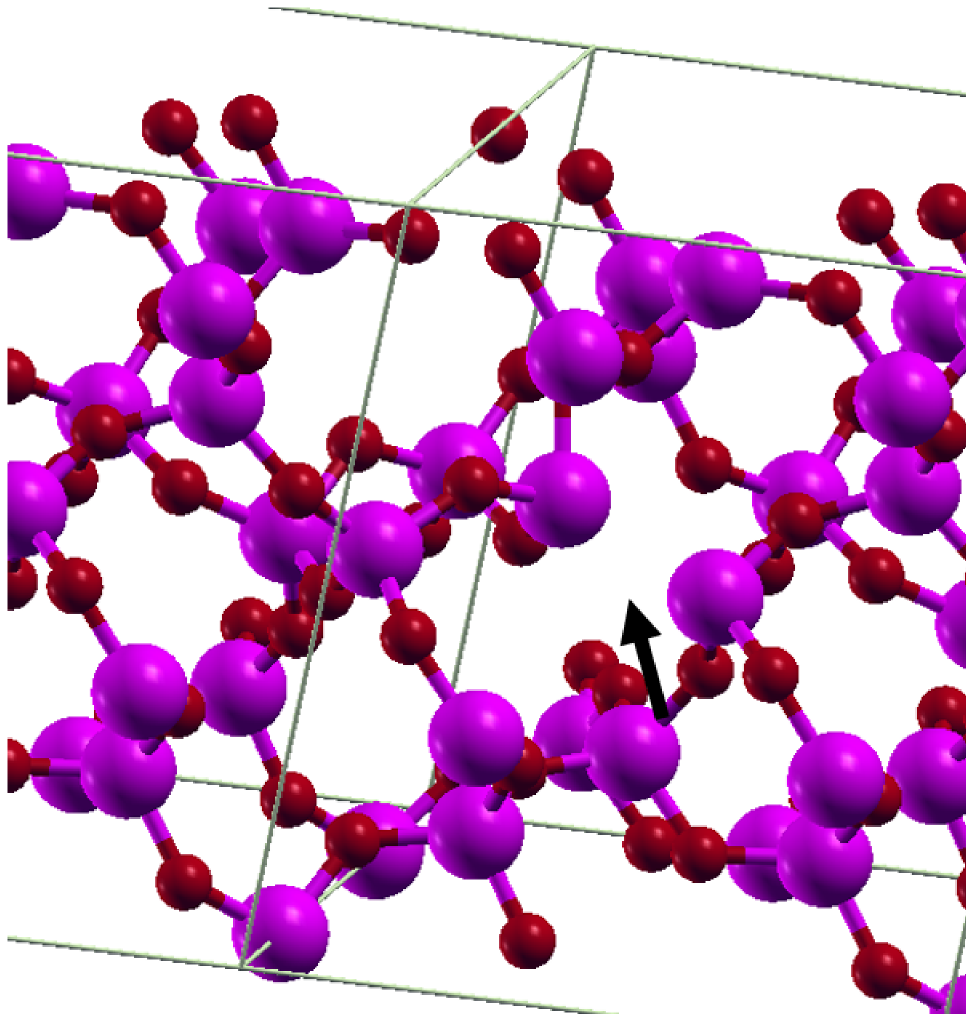

Figure 3.11: 71 atom supercell of amorphous GeO_2 with an oxygen vacancy (indicated with black arrow). Ge atoms are labeled with purple and O atoms are labeled with red.

the 3 Ge atoms it bonds to, and the 9 other O atoms bonded to those Ge atoms (3 O atoms each) were allowed to move during the calculation. To determine which atoms would be allowed to move, the atomic coordinates of the two original vacancy supercells were compared, and the overall distance between each corresponding pair of atoms was calculated. The atoms were sorted according to largest displacement and a cut off was set when the displacement fell down by a factor of 5, with only the atoms with a larger overall displacement being allowed to move. Since the other atoms were not allowed to move during the calculation, the coordinates of those atoms in the initial and final configurations has to be equal. To accomplish this, the average positions for the fixed atoms between the original two vacancy supercells were calculated and used as input for the initial and final configurations. The configurations were then relaxed while holding the necessary atoms fixed. These relaxed configurations were then used as input for the NEB.

The NEB for the oxygen vacancy migration reaction pathway was set up using 5 total images. An intermediate configuration was provided, which took the average of the initial and final configuration coordinates, except for the hopping O atom which was placed such that with the initial and final positions, an arc was swept out with the middle Ge atom as the pivot. The calculated reaction pathway is depicted in Fig.3.12. A barrier height of 2.5 eV was found for the reaction, which agrees well with previous calculations [15].

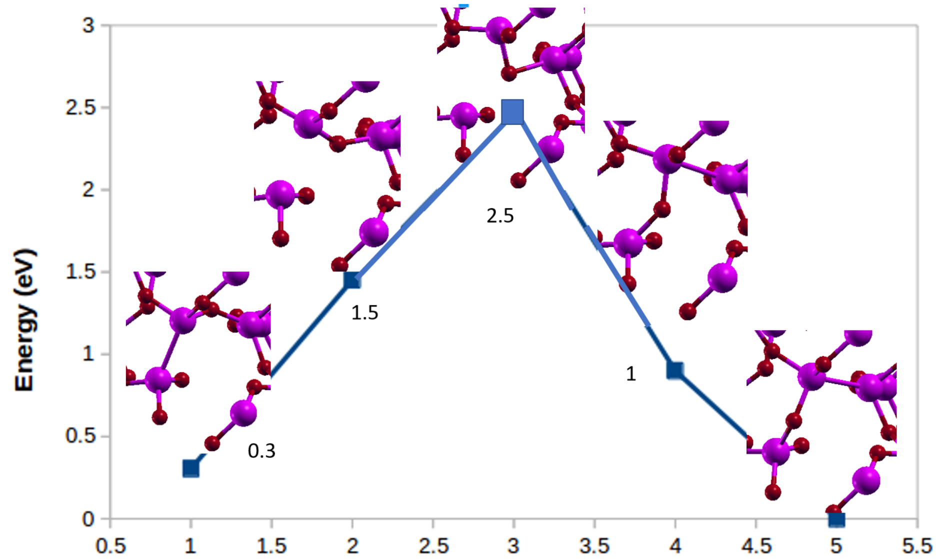

Figure 3.12: Reaction pathway of oxygen vacancy migration. Steps in the reaction pathway are plotted according to energy difference relative to the final configuration. Energy barrier is given at maximum. Ge atoms are labeled with purple and O atoms are labeled with red.

3.2.2.2 Fluorine Passivation of Oxygen Vacancy

To passivate oxygen vacancies, fluorine passivation was considered. While hydrogen is the primary element used for passivation of silicon-based defects, previous studies [12] [8] [13] have indicated that hydrogen is ineffective at passivating defects in germanium. In the case of fluorine, previous experiments have confirmed that use of fluorine in germanium interface fabrication has lead a reduction in interface defects and other undesirable qualities [8] [10] [11]. However, the use of theoretical techniques, such as DFT, in passed studies have lead to conflicting results and have so far failed to fully explain how fluorine is incorporated to reduce defects [4] [11]. More DFT studies were carried out to understand the behavior of fluorine in the

oxide network and by the interface.

Initially, both hydrogen and fluorine were used to simulate vacancy passivation to compare effectiveness. The previously simulated 71 atom supercells of amorphous GeO_2 containing a single oxygen vacancy were used. Either an H_2 or an F_2 molecule was then added to the cell and placed in various configurations in close proximity to the vacancy, a sample of initial configurations is shown in Fig.3.13. The various configurations were used to probe the possible ways that fluorine and hydrogen incorporate into the defected oxide network. The structures were relaxed using an energy cutoff of 400 eV, with k-space calculations approximated with the Gamma point, and converged once all force components were below 0.5 eV/Å. The final configurations are depicted in Fig.3.14.

As shown, in both cases there were two distinct final configurations, categorized as a proper vacancy passivation and an improper passivation. In the case of proper passivation, the additional atoms formed bonds with the target Ge atoms, and the Ge-Ge bond of the vacancy broken. In the case of the improper passivation, one of the added atoms formed a bond with a target Ge atom, but the other bonded with one of the neighboring oxygen atoms, causing the oxygen atom to break away from the other target Ge atom, leaving it in a doubly coordinated stated. This is an undesirable configuration, as there are still dangling bonds remaining, and thus still acts as a charge trap.

In the case of H, the improper passivation was more energetically favorable than the proper passivation by 0.2 eV and supports the previous observations that charge traps and defects still existed after H passivation.

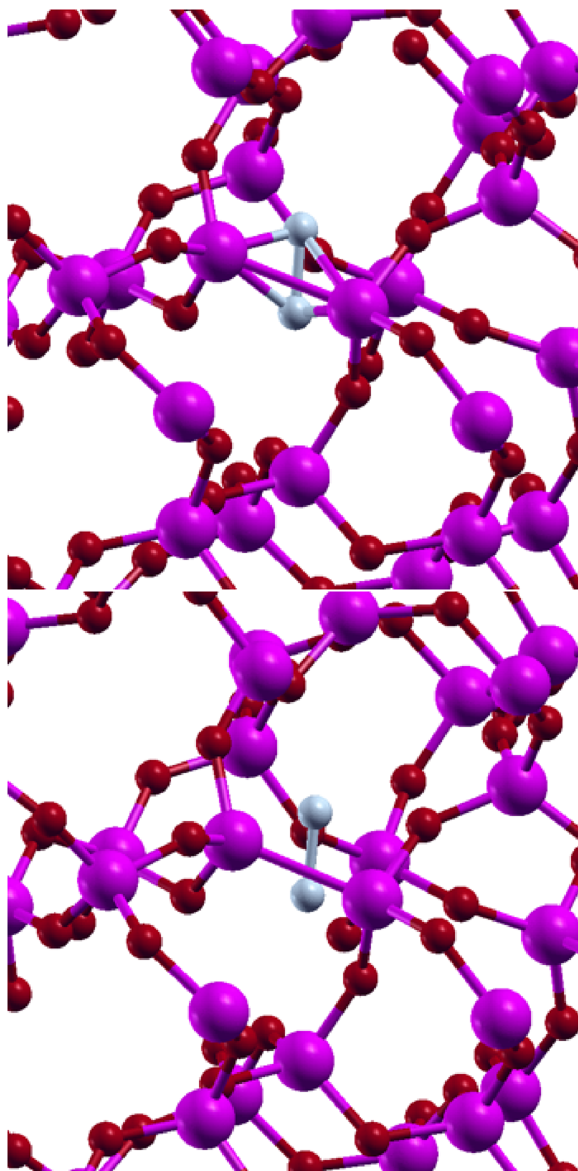

Figure 3.13: Sample of initial configurations of F_2 by an oxygen vacancy in a 71 atom amorphous GeO_2 supercell with varying distance to the defect. Ge atoms are labeled in purple, O atoms in red, F atoms in silver. Analogous initial configurations were used in the H_2 case.

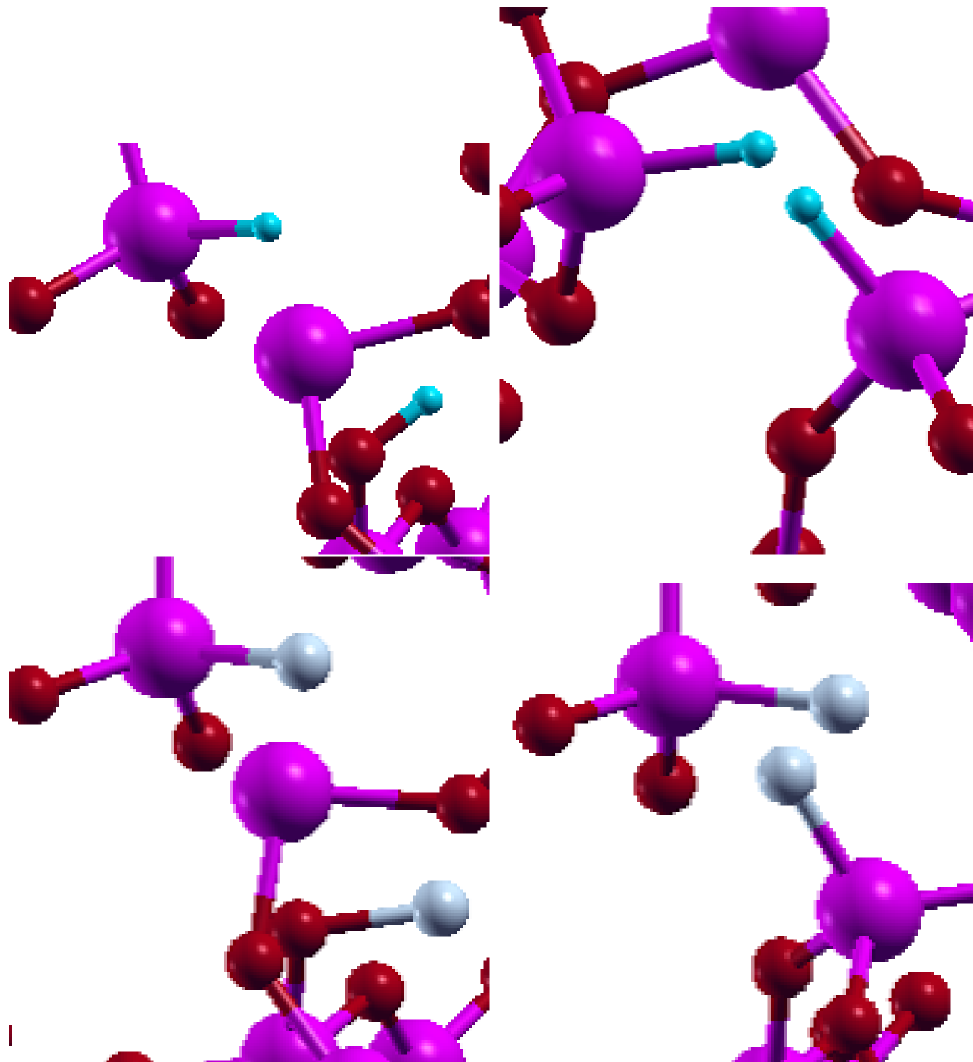

Figure 3.14: Close up of target region of final relaxed structures of 2 H (top) or F (bottom) atoms incorporated into a defected 71 atom amorphous GeO_2 supercell. Ge atoms are labeled in purple, O atoms in red, F atoms in silver, H atoms in blue. On the left are the improper passivations, where one of the H (or F) atoms are bonded to an O atom, leaving a doubly-coordinated Ge atom. On the right are the proper passivations, with the Ge-Ge bond eliminated and replaced with Ge-H (or F) bonds.

In the case of F, the proper passivation was more energetically favorable than the improper passivation by 4 eV. With such a large energy difference, the improper passivation will essentially not occur, and may be one of the reasons why fluorine is effective at reducing defect and trap densities for GeO_2.

The DFT simulations support the previous observations that H is an ineffective passivant while F is an effective passivant for defects in GeO_2. For this reason, more DFT simulations were carried out to understand the behavior of fluorine in GeO_2.

To further understand if fluorine would be effective at passivating oxygen vacancies, DFT simulations were run to compare fully passivated and half passivated vacancies using fluorine. One or two fluorine atoms were added to the 71 atom amorphous GeO_2 supercell with an oxygen vacancy, for the half and fully passivated cases, respectively. DFT calculations were performed using a 400 eV plane wave energy cut off, and Brillouin zone calculations were approximated using 2 k-space points. To account for unpaired electrons, magnetization and the electron spin density was calculated using a spin polarized PBE functional, and the structure was relaxed once the force components on each atom were below 0.5 eV/Å. The final relaxed structures are shown in Fig.3.15

The results of the energy calculations of the final structures shows that fully passivated vacancies are more energetically favorable than half passivated vacancies. The energy of 2 half passivated supercells is 1.2 eV greater than the energy of 1 fully passivated supercell plus a bulk GeO_2 supercell, indicating that half passivated vacancies are not thermodynamically favorable, and their formation will then be limited by the diffusion of fluorine through the oxide network.

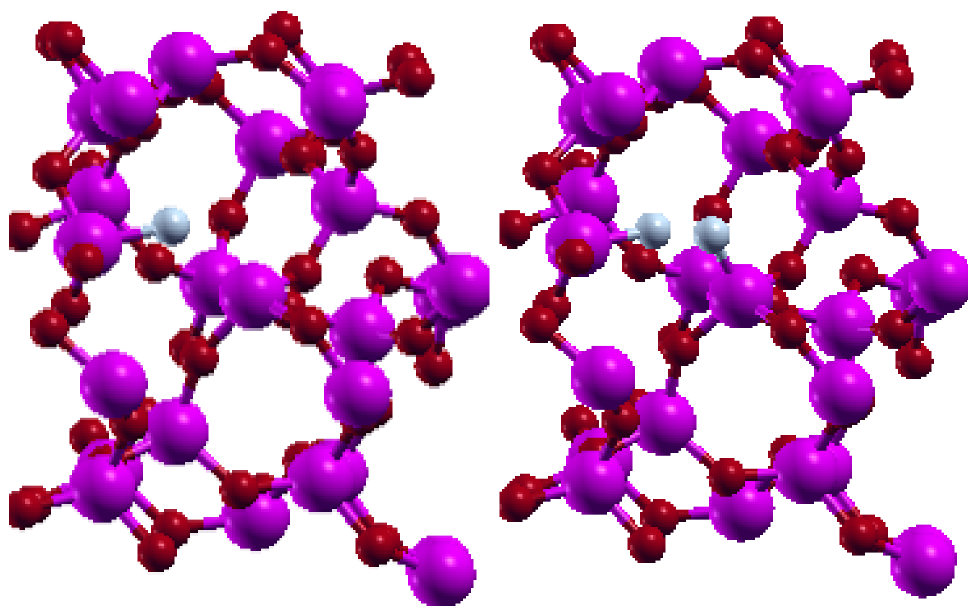

Figure 3.15: Final relaxed structure of 72 (73) atom amorphous GeO_2 supercell with a half (fully) passivated oxygen vacancy by 1 (2) F atom(s). Ge atoms are labeled in purple, O atoms in red, F atoms in silver. On the left is the half passivated vacancy, on the right is the fully passivated vacancy.

3.2.2.3 Diffusion of Fluorine in GeO_2

While fluorine has been found to be an effective passivant during GeO_2 fabrication, the degree of effectiveness varies across experiments. To determine what some optimal parameters and conditions for fabrication are, DFT simulations of fluorine incorporated into various GeO_2 supercells were carried out.

One of the crucial components for understanding the behavior of fluorine inside the GeO_2 network during fabrication is how fluorine diffuses through the oxide network. The majority of the fluorine atoms inside the network will not be near any defects and will just be interacting with the oxide network. While there are numerous experiments that have made use of fluorine during Ge device fabrication, no study as of yet has explored how fluorine interacts with the oxide network, or how it diffuses. To determine how fluorine diffuses, DFT simulations were first carried out to determine how fluorine atoms relax inside amorphous GeO_2.

Fluorine atoms were added to 72 atom and 144 atom amorphous GeO_2 supercells, with either 1 or 2 atoms fluorine atoms included. The fluorine atoms were set in various initial configurations within the cell, either close to Ge atoms, close to O atoms, or placed in the middle of the interstitials. The structures were then relaxed using an energy cut off of 400 eV, and the Brillouin zone calculations were approximated using two k-space points. To account for the effects of unpaired electrons, magnetization was included and the electron spin density was calculated. The structure was converged once all force components were below 0.5 eV/Å.

The results of the simulations indicate that there are two configurations for

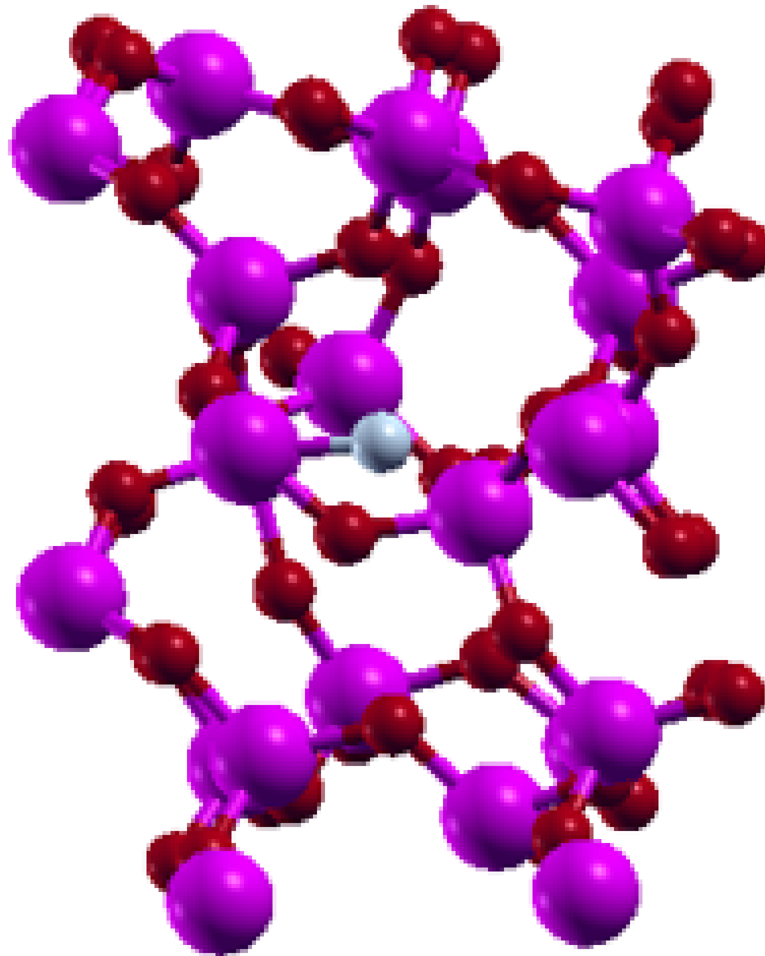

Figure 3.16: Final relaxed structure of an F atom placed into a 72 atom amorphous GeO_2 supercell. Ge atoms are labeled in purple, O atoms in red, F atoms in silver. The F atom has incorporated into the oxide network via bonding with Ge atoms. The Ge atoms are 5-coordinated.

how fluorine resides in amorphous GeO_2: Either in the interstitials of the network, or incorporated into the network via bonding with a Ge atom. The results of the energetics of these configurations show that the interstitials are unstable equilibrium for F atoms, whereas the incorporated configurations are stable equilibrium. In the incorporated configurations, the magnetization calculation revealed that an unpaired electron remained, with a net calculated magnetization of 0.5 Bohr magnetons. This indicates that the F atom is still electrically reactive in the bonded state and will likely act as a charge trap or react with other elements added during fabrication. However, since previous experiments using fluorine in Ge device fabrication have not observed an increase in overall charge traps, the stability of the charged fluorine states will need to be investigated. The final configurations are depicted for the case of 2 F atoms in Fig.3.17. In the case of 1 F atom, none of the relaxed structures converged to the interstitial configuration, indicating the unstable nature of the equilibrium.

Another result of the simulations is that the F atoms will tend to separate through the network instead of forming clusters. This was established by comparing the energetics of the relaxed supercells with 1 or 2 F atoms, respectively, with all F atoms in the incorporated configurations. The final energy of the supercells with two F atoms incorporated was 1.1 eV higher than two supercells each with one F atom incorporated, indicating it would take about 1.1 eV to bring incorporated F atoms in proximity. Such a large energy difference is a clear sign of a large repulsive force between incorporated F atoms.

In conclusion, a number of atomic configurations related to fluorine passivation

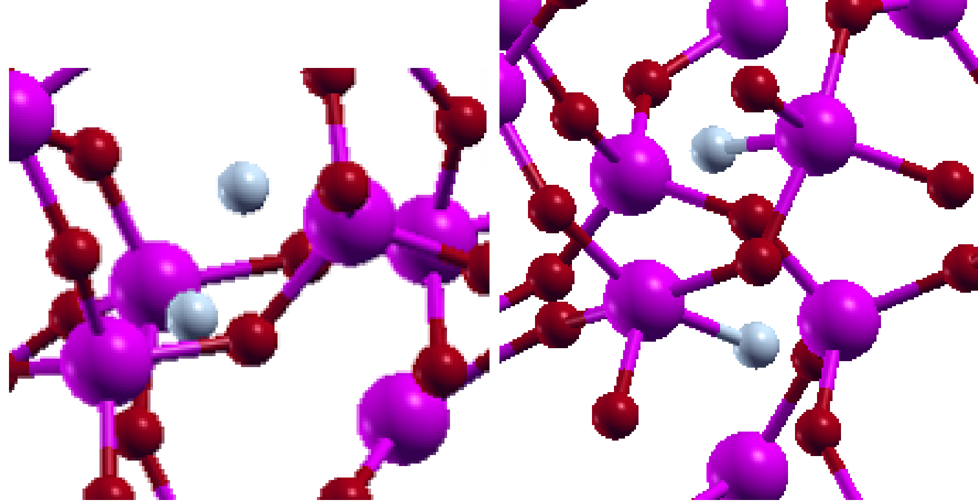

Figure 3.17: Close up of final relaxed structure of 2 F atoms placed into a 72 atom amorphous GeO_2 supercell. Ge atoms are labeled in purple, O atoms in red, F atoms in silver. On the left image the F atoms are relaxed in interstitial configurations, which were found to be unstable for the 1 F atom case. On the right, the F atoms have incorporated into the oxide network via bonding with Ge atoms. The Ge atoms are 5-coordinated.

of oxygen vacancy defects, and fluorine diffusion through GeO_2, were simulated using DFT with the energy of each configuration calculated as well.

3.3 Future Research

For the future, the above DFT results could be used as input into a Monte Carlo simulation. The diffusion of fluorine atoms through the oxide network could be simulated and optimal fabrication parameters, such as temperature, duration of steps, partial pressures for oxygen, fluorine, and other gases used, and others, could be determined in order to reduce defect density and/or surface roughness.

Chapter A: Density Functional Theory

A.1 Born-Oppenheimer Approximation

The first step in solving for the electron density is separating the electron motion from the motion of the atomic nuclei in the Schrodinger equation. This is accomplished by invoking the Born-Oppenheimer Approximation [57], which posits that the electron cloud evolves much quicker than the atomic nuclei, so that the nuclei essentially freeze out and the electrons see a static potential background. This assumption is perfectly valid for most quantum chemistry applications.

The approximation is expressed mathematically by applying separation of variables to the Schrodinger Equation as follows:

Express the wavefunction as:

$$\Psi(r_1, .., r_N, R_1, ..., R_M) = \Phi(r_1, ..., r_N)\chi(R_1, ..., R_M) \tag{A.1}$$

where Φ is the electronic wavefunction and χ is the nuclear wavefunction.

Then re-write the Hamiltonian

$$H(r, R) = H_N(R) + H_e(r, R) \tag{A.2}$$

where H_N is the nuclear kinetic energy term and H_e contains the remaining terms. This decouples the Schrodinger Equation into:

$$E_e(R)\Phi(r) = H_e(r,R)\Phi(r) \tag{A.3}$$

$$E\chi(R) = (H_N(R) + E_e(R))\chi(R) \tag{A.4}$$

The first equation describes the electronic wavefunction and treats the nuclear coordinates as parameters, expressing the electronic energy (chemical energy) as a function of the nuclear coordinates. Once the energy function has been determined, the second equation can be solved, which describes the nuclear wavefunction by treating the chemical energy as the potential energy. The first equation is the equation that will be considered for the remainder of the paper, where the quantity of interest is the electron density and energy of an atomic configuration in terms of the atomic coordinates.

A.2 Hohenberg-Kohn Theorems

The next step is replacing the electronic Hamiltonian and electronic wavefunction from the previous section with an energy functional and the electron density. The Hohenberg-Kohn Theorems [16], assert that no information is lost here, and that there is a one-to-one correspondence between wavefunction and electron density, so that every Hamiltonian has a unique solution in terms of the density. Thus the energy of the system can be expressed as a functional of the density, and can be broken up into two components:

$$E[\rho] = F[\rho] + V_{ext}[\rho] \tag{A.5}$$

where V_{ext} is the external potential created by the static atomic nuclei, and F is the universal functional, which is the same for all systems and accounts for the kinetic energy and electron-electron interactions. Each atomic configuration produces an energy functional, and the solution is the electron density that minimizes the functional. Unfortunately, the exact form of the universal functional is not known and approximate functionals have to be constructed, resulting in a variety of functionals best suited for different applications depending on the situation.

Bibliography

[1] Akira Toriumi and Tomonori Nishimura 2018 Jpn. J. Appl. Phys. 57 010101

[2] Binder, Jan Felix., and Alfredo Pasquarello. *Electronic and Structural Properties of the Ge/GeO Interface through Hybrid Functionals.* These Ecole polytechnique federale de Lausanne EPFL, no 5363 (2012), Programme doctoral Physique, Faculte des sciences de base SB, Institut de theories des phenomenes physiques ITP (Chaire de simulation a lechelle atomique CSEA). Dir.: Alfredo Pasquarello, 2012.

[3] Choong Hyun Lee et al., ECS Tran., 19 (1) 165-173 (2009)

[4] L. Tsetseris, and S. T. Pantelides, Appl. Phys. Lett. 95, 262107 (2010); https://doi.org/10.1063/1.3280385

[5] K. Kita, S. Suzuki, H. Nomura, T. Takahashi, T. Nishimura, and A.Toriumi:Jpn. J. Appl. Phys.47(2008) 2349

[6] Sheng Kai Wang et al., 2011 Jpn. J. Appl. Phys. 50 10PE04

[7] Sheng Kai Wang et al., 2011 Jpn. J. Appl. Phys. 50 04DA01

[8] Lee, Hyun, et al. *Characteristics improvement of HfO2/Ge gate stack structure by fluorine treatment of germanium surface.* Applied Surface Science, vol. 254, no. 21, 30 Aug. 2008, pp. 69326936., doi:10.1016/j.apsusc.2008.04.110.

[9] C. H. Lee, T. Nishimura, K. Nagashio, K. Kita and A. Toriumi, *"High-Electron-Mobility hboxGe/GeO_2 n-MOSFETs With Two-Step Oxidation,"* in IEEE Transactions on Electron Devices, vol. 58, no. 5, pp. 1295-1301, May 2011.doi: 10.1109/TED.2011.2111373

[10] R. Xie et al., *"High mobility high-k/Ge pMOSFETs with 1 nm EOT -New concept on interface engineering and interface characterization,"* 2008 IEEE International Electron Devices Meeting, San Francisco, CA, 2008, pp. 1-4.doi: 10.1109/IEDM.2008.4796703

[11] Xie, R., et al. (2008). 2008 IEEE International Electron Devices Meeting.

[12] AfanasEv, V. V., et al. (2005). APL, 87(3), 032107

[13] Weber, J. R et al. (2007) APL, 91(14), 142101

[14] Deal, B. E., Grove, A. S. (1965). General Relationship for the Thermal Oxidation of Silicon. Journal of Applied Physics, 36(12), 3770-3778. doi:10.1063/1.1713945

[15] Li, H., Robertson, J. (2017). Germanium oxidation occurs by diffusion of oxygen network interstitials. Applied Physics Letters, 110(22), 222902. doi:10.1063/1.4984805

[16] Hohenberg, P., Kohn, W. (1964). Inhomogeneous Electron Gas. Physical Review, 136(3B). doi:10.1103/physrev.136.b864

[17] Kohn, W., Sham, L. J. (1965). Self-Consistent Equations Including Exchange and Correlation Effects. Physical Review, 140(4A). doi:10.1103/physrev.140.a1133

[18] R.Crowell and S.M. Sze, Current transport in metal-semiconductor barriers, Solid-State Electron., vol.9,pp. 1035-1047,1966

[19] http://www.phys.uni-paderborn.de/ rauls/diss/thesis.pdf

[20] Traversa, F. L., Bertazzi, F., Bonani, F., Guerrieri, S. D., Ghione, G., Perez, S., . . . Gonzalez, T. (2010). A Generalized Drift-Diffusion Model for Rectifying Schottky Contact Simulation. IEEE Transactions on Electron Devices, 57(7), 1539-1547. doi:10.1109/ted.2010.2047909

[21] Adams, J., Tang, T. (1986). A revised boundary condition for the numerical analysis of Schottky barrier diodes. IEEE Electron Device Letters, 7(9), 525-527. doi:10.1109/edl.1986.26460

[22] Preezant, Y., Tessler, N. (2003). Self-consistent analysis of the contact phenomena in low-mobility semiconductors. Journal of Applied Physics, 93(4), 2059-2064. doi:10.1063/1.1539534

[23] Akturk, A., Salemi, S., Goldsman, N., Potbhare, S., Lelis, A. (2011). Density functional theory based simulation of carrier transport in silicon carbide and silicon carbide-silicon dioxide interfaces. 2011 International Conference on Simulation of Semiconductor Processes and Devices. doi:10.1109/sispad.2011.6035064

[24] Salemi, S., Goldsman, N., Ettisserry, D. P., Akturk, A., Lelis, A. (2013). The effect of defects and their passivation on the density of states of the 4H-silicon-carbide/silicon-dioxide interface. Journal of Applied Physics, 113(5), 053703. doi:10.1063/1.4789615

[25] Dek, P., Knaup, J., Thill, C., Frauenheim, T., Hornos, T., Gali, A. (2008). The mechanism of defect creation and passivation at the SiC/SiO2 interface. Journal of Physics D: Applied Physics, 41(4), 049801-049801. doi:10.1088/0022-3727/41/4/049801

[26] INTEGRATED MODELING OF RELIABILITY AND PERFORMANCE OF 4H-SILICON CARBIDE POWER MOSFETS USING ATOMISTIC AND DEVICE SIMULATIONS (Unpublished master's thesis). Thesis / Dissertation ETD. (2015).

[27] Tilak, V., Matocha, K., Dunne, G. (2007). Electron-Scattering Mechanisms in Heavily Doped Silicon Carbide MOSFET Inversion Layers. IEEE Transactions on Electron Devices, 54(11), 2823-2829. doi:10.1109/ted.2007.906929

[28] Darmody, C., Goldsman, N. (2018). The intrinsic atomic-level surface roughness mobility limit of 4H-SiC. Journal of Applied Physics, 124(10), 105702. doi:10.1063/1.5042765

[29] Pennington, G., Potbhare, S., Goldsman, N., Mcgarrity, J., Lelis, A. (n.d.). Impact of Surface Steps on the Roughness Mobility in 4H-SiC. 2005 International Semiconductor Device Research Symposium. doi:10.1109/isdrs.2005.1596021

[30] S. Wang et. al.,Phys. Rev. Lett. 98, 026101 (2007)

[31] S. Wang, M. DiVentra, S.G. Kim, and S.T.Pantelides,Phys. Rev. Lett. 86,5946 (2001)

[32] Y. Hijikata, H. Yaguchi, and S.Yoshida, Applied Physics Express 2,021203(2009)

[33] Taillon, J. A., Yang, J. H., Ahyi, C. A., Rozen, J., Williams, J. R., Feldman, L. C., . . . Salamanca-Riba, L. G. (2013). Systematic structural and chemical

characterization of the transition layer at the interface of NO-annealed 4H-SiC/SiO2 metal-oxide-semiconductor field-effect transistors. Journal of Applied Physics, 113(4), 044517. doi:10.1063/1.4789924

[34] Home, www.iue.tuwien.ac.at/phd/rescher/Introduction.html.

[35] 5-2-2-1 SiC Crystallography: Important Polytypes and Definitions 5.Silicon Carbide Technology Knowledge Compound Semiconductor Wafer. Silicon Wafer, www.siliconcarbidewafer.com/SiC-Crystallography–Important-Polytypes-and-Definitions.html.

[36] 3.2.2 Effective Masses and Intrinsic Carrier Density, www.iue.tuwien.ac.at/phd/ayalew/node62.html.

[37] Feng, Zhe Chuan. SiC Power Materials: Devices and Applications. Springer, 2011.

[38] Goiran, M, et al. Cyclotron Resonance of Electrons in 6H-SiC in High Magnetic Fields up to 50T. Physica B: Condensed Matter, vol. 246-247, 1998, pp. 270273., doi:10.1016/s0921-4526(97)00913-7.

[39] Keller, Stacia, et al. Recent Progress in Metal-Organic Chemical Vapor Deposition of (0001) N-Polar Group-III Nitrides. Semiconductor Science and Technology, vol. 29, no. 11, 2014, p. 113001., doi:10.1088/0268-1242/29/11/113001.

[40] Pennington, G., and N. Goldsman. Self-Consistent Calculations For n-Type Hexagonal SiC Inversion Layers. Journal of Applied Physics, vol. 95, no. 8, 2004, pp. 42234234., doi:10.1063/1.1687977.

[41] Vetter, Ulrich. (2019). Lanthanide doped wide band gap semiconductors [Elektronische Ressource] : intra-4f luminescence and lattice location studies /.

[42] Dolny, Gary, et al. Multi-Level Trap Assisted Tunneling Model for the Field and Temperature Dependence of SiC-JBS Reverse Leakage Current. Materials Science Forum, vol. 924, 2018, pp. 601604., doi:10.4028/www.scientific.net/msf.924.601.

[43] Rengel, Ral, et al. Injected Current and Quantum Transmission Coefficient in Low Schottky Barriers: WKB and Airy Approaches. IEEE Electron Device Letters, vol. 28, no. 2, 2007, pp. 171173., doi:10.1109/led.2006.889511.

[44] Jirauschek, Christian. Accuracy of Transfer Matrix Approaches for Solving the Effective Mass Schrdinger Equation. IEEE Journal of Quantum Electronics, vol. 45, no. 9, 2009, pp. 10591067., doi:10.1109/jqe.2009.2020998.

[45] Li, Jin-Lan, et al. Influence of Deep Defects on Electrical Properties of Ni/4H-SiC Schottky Diode. Chinese Physics B, vol. 28, no. 2, 2019, p. 027303., doi:10.1088/1674-1056/28/2/027303.

[46] L. M. Porter and R. F. Davis, Mater. Sci. Eng., B 34, 83 1995

[47] A. Itoh and H. Matsunami, Phys. Status Solidi A 162, 389 1997

[48] Ewing, D. J., Porter, L. M., Wahab, Q., Ma, X., Sudharshan, T. S., Tumakha, S.,Brillson, L. J. (2007). Inhomogeneities in Ni4H-SiC Schottky barriers: Localized Fermi-level pinning by defect states. Journal of Applied Physics, 101(11), 114514. doi:10.1063/1.2745436

[49] Neudeck, P. G., Spry, D. J., Trunek, A. J. (2006). Measurements of Breakdown Field and Forward Current Stability in 3C-SiC pn Junction Diodes Grown on Step-Free 4H-SiC. Materials Science Forum, 527-529, 1335-1338. doi:10.4028/www.scientific.net/msf.527-529.1335

[50] SiCWhat are SiC Semiconductors?. (n.d.). Retrieved from https://www.rohm.com/electronics-basics/sic/what-are-sic-semiconductors

[51] Neamen, D. A. (2008). An introduction to semiconductor devices. Boston, MA: McGraw-Hill Higher Education.

[52] (n.d.). Retrieved from https://ecee.colorado.edu/ bart/book/barlow.htm

[53] Chapter 3: Metal-Semicond. Junctions. (n.d.). Retrieved from https://ecee.colorado.edu/ bart/book/book/chapter3/ch34.htm3442

[54] Nanoscale Transport 2016. (n.d.). Retrieved from http://www.hri.res.in/ nanotr16/notes/

[55] Mitchell Gross, Aysanew Abate, Dr. Akin Akturk and Dr. Zeynep Dilli, private communication.

[56] W. P. Harrison (1989) [1980]. Electronic Structure and the Properties of Solids (Reprint ed.). Dover Publications. pp. 158 ff. ISBN 0-486-66021-4.

[57] P. Giannozzi et al., J. Phys.:Condens. Matter 21 395502 (2009); URL http://www.quantum-espresso.org